Electric Power Systems Research 163 (2018) 196–210

Contents lists available at ScienceDirect

Electric Power Systems Research

journal homepage: www.elsevier.com/locate/epsr

Modeling, control, and reduced-order representation of modular multilevel converters

Andres E. Leon[a,*], Santiago J. Amodeo[a,b]

[a] Instituto de Investigaciones en Ingeniería Eléctrica (IIIE) 'Alfredo Desages', Universidad Nacional del Sur (UNS)-CONICET, Avda. Alem 1253, Bahía Blanca 8000, Argentina

[b] ElectroAMSA Company, Mascarello 3560, Ingeniero White 8103, Argentina

ARTICLE INFO

Keywords:
Modular multilevel converter (MMC)
Power system simulations
Reduced-order model
Electromechanical transient analysis
Control systems

ABSTRACT

This paper presents a reduced-order model of the modular multilevel converter (MMC) for electromechanical transient simulations and small-signal analysis. The MMC model is firstly developed in detail; then, simplifications are introduced to reduce it to eleventh- and fourth-order models. The dynamic behaviors of the traditional voltage-source converter and the MMC are also compared. A thorough description of the MMC control system is presented including the inner current control loops, the outer voltage control loops, and the strategy to balance the floating capacitor voltages. Control systems in continuous- and discrete-time domains are given to enable their use in power system simulations and in practical implementations, respectively. Several tests are performed to compare the steady-state and transient response of the detailed and the reduced models. The results show that the fourth-order reduced model can properly capture the input-output dynamics of a complete MMC and significantly reduce the computational cost of large-scale power system simulations with multiple ac/dc converter stations.

1. Introduction

The first ac/dc converter stations based on voltage-source converters (VSCs) could not reach the high-power and high-voltage levels of the conventional line-commutated converters. VSC stations able to manage thousands of megawatts and to transmit at the highest voltage levels have recently become possible with the development of the modular multilevel converter (MMC) [1]. Many applications, such as multi-terminal dc systems, integration of offshore wind farms, and interconnection of asynchronous ac systems, are driven by these power converter developments [2–4]. To assess the impact of these installations on the system by means of small-signal and transient stability analyses, the converter stations are often represented by the traditional two- or three-level VSC [5–8], although multilevel converters such as the MMC are more appropriate for these power and voltage ranges. The characteristics of converter stations based on the MMC are not accurately described by the traditional VSC model. Both converter models have a similar representation on the ac side but a different one on the dc side, where the traditional VSC behaves like a voltage source and the MMC behaves like a current source [9].

Detailed models of the MMC with explicit representation of all submodule capacitors are not suitable for the stability analysis of large-scale power systems due to their high computational cost and the required small simulation time steps [2]. On the other hand, another issue should be considered in detailed models. Unlike to what happens in the traditional VSC, the alternating arm currents of the MMC cause ripples in the submodule capacitor voltages during normal steady-state operation [10]. The modeling of these ripples can be a drawback in power system stability analyses that require a constant equilibrium point to compute eigenvalues and small-signal properties [11]. To simplify the MMC representation, averaged or continuous models have been proposed in [12–15] but, as the arm capacitor voltage ripple is still modeled, these models do not have a constant equilibrium point; therefore, they cannot be used to perform small-signal (modal) analysis. To solve this issue, in [16–19], different rotating reference frames are defined and, after neglecting some terms, the oscillating variables are transformed to constant values. As in the averaged models, these approaches represent the individual arm voltages that require the inclusion of the circulating current control and the inter-arm voltage balancing algorithm in their control systems.

On the other hand, reduced models are usually considered in large-scale power systems where electromechanical transients are studied and the MMC is analyzed from an input-output point of view [20]. These models reduce the amount of state variables by assuming that the

* Corresponding author.
E-mail address: aleon@iiie-conicet.gob.ar (A.E. Leon).

https://doi.org/10.1016/j.epsr.2018.05.024
Received 10 November 2017; Received in revised form 16 February 2018; Accepted 23 May 2018

balancing of the submodule capacitor voltages is internally performed by the converter control system. In [21–26], reduced models have been proposed, but they do not model the MMC inductive behavior on the dc side, which was solved in [27–31] by adding a dc-side inductance. However, in these papers, the MMC representation is derived from a power balance equation, resulting in an RLC circuit that does not show the effect of the zero-sequence modulation index on the dc side. As shown in [32], the dc-side dynamics depends on the zero-sequence modulation index, and this has an impact on the accuracy of the transient response. This distinctive characteristic of the MMC also allows to independently control the total converter energy and the dc-bus voltage.

The contributions of this work can be summarized as follows: (1) the modeling and control of the MMC are described in detail –a step-by-step derivation is provided; (2) a reduced-order model of the MMC suitable for transient and small-signal stability studies is developed –this model allows to design the outer control loops in networks with multiple MMCs, as well as to speed up large-scale power system simulations; and (3) a comparison between the traditional VSC and the MMC is also performed to show their distinctive dc-side dynamics.

The paper is organized as follows. In Sections 2 and 3, a comprehensive model of the current and voltage dynamics is obtained directly from the MMC electrical circuit. The current control loops and the capacitor voltage balancing are described in Sections 4 and 5, respectively. The reduced MMC model is introduced in Section 6, where a comparison with the traditional VSC is also discussed. The inner and outer control loops of the reduced model are presented in Section 7. Section 8 evaluates the performance of the proposed control systems and compares the detailed and reduced models using the 401-level MMC of the France-Spain electrical interconnection (INELFE) project [33]. Finally, conclusions are drawn in Section 9.

2. MMC currents

2.1. Basic equations of the MMC electrical circuit

Applying the Kirchhoff's voltage law to the loops connecting the points *M–p–z–M* and *M–n–z–M* of the circuit shown in Fig. 1(b), the following equations are obtained, respectively

$$\frac{v_{\mathrm{dc}}}{2} - v_p^z + R_s i_p^z + L_s \dot{i}_p^z = v_{\mathrm{zM}} \tag{1}$$

$$-\frac{v_{\mathrm{dc}}}{2} + v_n^z - R_s i_n^z - L_s \dot{i}_n^z = v_{\mathrm{zM}} \tag{2}$$

where M is the fictitious dc-side midpoint, p and n are the positive and negative nodes, and the point $z = \{a, b, c\}$ is the midpoint of a generic converter phase-leg. The rest of the variables and parameters are defined in Fig. 1(b). Adding and subtracting (1) and (2) result in

$$v_n^z - v_p^z + R_s(i_p^z - i_n^z) + L_s(\dot{i}_p^z - \dot{i}_n^z) = 2v_{\mathrm{zM}} \tag{3}$$

$$v_{\mathrm{dc}} - v_p^z - v_n^z + R_s(i_p^z + i_n^z) + L_s(\dot{i}_p^z + \dot{i}_n^z) = 0. \tag{4}$$

Applying the Kirchhoff's voltage law to the loop *N–z–N* yields

$$v_g^z - R_e i_g^z - L_e \dot{i}_g^z = v_{\mathrm{zN}} \tag{5}$$

where N is the ac-side neutral point. On the other hand, applying the Kirchhoff's current law to the positive and negative nodes of the MMC gives

$$i_{\mathrm{dc}} = i_p^a + i_p^b + i_p^c = \sum_{w=a,b,c} i_p^w \tag{6}$$

$$i_{\mathrm{dc}} = i_n^a + i_n^b + i_n^c = \sum_{w=a,b,c} i_n^w \tag{7}$$

whereas applying the Kirchhoff's current law to the midpoint of a phase-leg gives

$$i_g^z = i_p^z - i_n^z. \tag{8}$$

Unlike the traditional VSC, due to unequal voltages among the legs, the MMC has a current that can circulate within the three phases, in the following referred to as circulating current. This circulating current is independent of the ac and dc currents, and it is not seen in the output terminals of the converter. The arm currents can be written as a function of the above three currents as follows [34]

$$i_p^z = \frac{i_{\mathrm{dc}}}{3} + \frac{i_g^z}{2} + i_{\mathrm{cir}}^z \tag{9}$$

$$i_n^z = \frac{i_{\mathrm{dc}}}{3} - \frac{i_g^z}{2} + i_{\mathrm{cir}}^z \tag{10}$$

where it has been assumed that the dc current is equally divided among the three legs of the converter and that the ac current is equally divided between the two arms of a leg. This assumption is reasonable because, under normal operating conditions, the impedance of each arm is similar [35]. In (9) and (10), the circulating current is the same for both arms of a leg because, by definition, this current flows inside the converter, and it also verifies

$$i_{\mathrm{cir}}^a + i_{\mathrm{cir}}^b + i_{\mathrm{cir}}^c = 0. \tag{11}$$

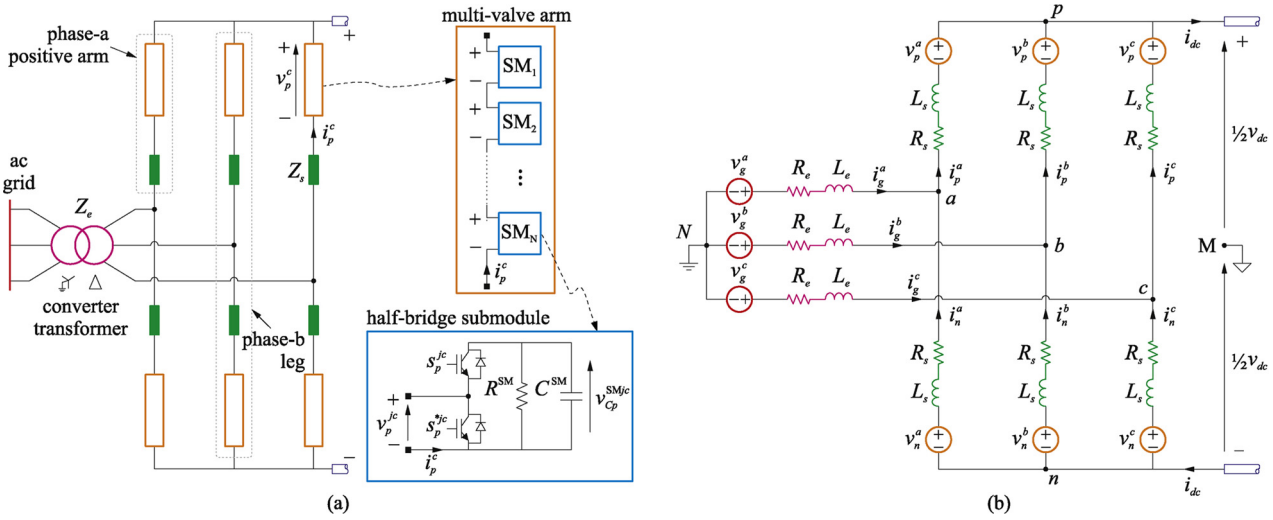

Fig. 1. Topology of the MMC. (a) Detail of the converter arm. (b) Equivalent electrical circuit.

2.2. DC current dynamics

To calculate the dynamics of the dc current, the following procedure is performed. First, the equation below is obtained by adding (6) and (7)

$$i_{dc} = \frac{1}{2}\sum_{w=a,b,c}(i_p^w + i_n^w). \tag{12}$$

Differentiating with respect to time (12) and using (1) and (2) give

$$\dot{i}_{dc} = \frac{1}{2L_s}\sum_{w=a,b,c}(v_p^w + v_n^w - R_s(i_p^w + i_n^w) - v_{dc}). \tag{13}$$

Then, distributing the summation of (13) and after some mathematical arrangements, the dynamic equation of the dc current results in

$$\frac{2}{3}L_s\dot{i}_{dc} = -\frac{2}{3}R_s i_{dc} - v_{dc} + \frac{1}{3}\sum_{w=a,b,c}(v_p^w + v_n^w). \tag{14}$$

2.3. AC current dynamics

The voltage between the points M and N can be written as follows

$$v_{MN} = v_{zN} - v_{zM}. \tag{15}$$

Using (15), the voltage v_{zN} is eliminated from (5),

$$v_g^z - R_e i_g^z - L_e\dot{i}_g^z - v_{MN} = v_{zM}. \tag{16}$$

Additionally, replacing (8) in (3) results in

$$v_n^z - v_p^z + R_s i_g^z + L_s\dot{i}_g^z = 2v_{zM}. \tag{17}$$

Then, substituting the voltage v_{zM} from (16) into (17), the dynamics of the ac currents is obtained as follows

$$L_t\dot{i}_g^z = -R_t i_g^z + v_g^z + \frac{1}{2}(v_p^z - v_n^z) - v_{MN} \tag{18}$$

where $R_t = R_e + \frac{1}{2}R_s$ and $L_t = L_e + \frac{1}{2}L_s$.

On the other hand, the voltage v_{MN} can be written as a function of the ac-side voltages and the arm voltages as described below. First, applying the Kirchhoff's voltage law to the loop N–z–p–M–N gives

$$v_g^z - R_e i_g^z - L_e\dot{i}_g^z - R_s i_p^z - L_s\dot{i}_p^z + v_p^z - \frac{v_{dc}}{2} = v_{MN}. \tag{19}$$

Then, adding (19) for the three phases $z = \{a, b, c\}$ and rearranging, we obtain

$$\sum_{w=a,b,c} v_g^w - R_s i_{dc} - L_s\dot{i}_{dc} + \sum_{w=a,b,c} v_p^w - \frac{3}{2}v_{dc} = 3v_{MN} \tag{20}$$

where (6) has been used. Because the star-delta transformer blocks the zero-sequence current [36], it has also been considered $\sum_{w=a,b,c} i_g^w = 0$. Finally, substituting (14) into (20), after some mathematical manipulations, yields

$$v_{MN} = \frac{1}{3}\sum_{w=a,b,c} v_g^w + \frac{1}{6}\sum_{w=a,b,c}(v_p^w - v_n^w). \tag{21}$$

The last expression will be used in following subsections.

2.4. Circulating current dynamics

The addition of (9) and (10) gives

$$i_p^z + i_n^z = 2\left(\frac{i_{dc}}{3} + i_{cir}^z\right). \tag{22}$$

Then, from (4) and considering (22), we obtain

$$v_{dc} - v_p^z - v_n^z + 2R_s\left(\frac{i_{dc}}{3} + i_{cir}^z\right) + 2L_s\left(\frac{\dot{i}_{dc}}{3} + \dot{i}_{cir}^z\right) = 0. \tag{23}$$

The term $\dot{i}_{dc}$ can be eliminated from (23) by using (14); therefore, the dynamics of the circulating currents results in

$$L_s\dot{i}_{cir}^z = -R_s i_{cir}^z + \frac{1}{2}(v_p^z + v_n^z) - \frac{1}{6}\sum_{w=a,b,c}(v_p^w + v_n^w). \tag{24}$$

2.5. Vector form of the current dynamics

Vector notation and $o\alpha\beta$ coordinates are considered in the following paragraphs to simplify the model representation. Expanding the summation term of (14), the dc current dynamics can be written as

$$\frac{2}{3}L_s\dot{i}_{dc} = -\frac{2}{3}R_s i_{dc} - v_{dc} + \mathbf{p}^T(\mathbf{v}_p^{abc} + \mathbf{v}_n^{abc}) \tag{25}$$

where the vectors $\mathbf{v}_p^{abc} = [v_p^a\ v_p^b\ v_p^c]^T$ and $\mathbf{v}_n^{abc} = [v_n^a\ v_n^b\ v_n^c]^T$ have been defined, and $\mathbf{p} = \frac{1}{3}[1\,1\,1]^T$. From the ac current dynamics (18) and considering (21) results in

$$\begin{aligned} L_t\dot{i}_g^z \;=\; & -R_t i_g^z + v_g^z + \tfrac{1}{2}(v_p^z - v_n^z) - \\ & \tfrac{1}{3}\textstyle\sum_{w=a,b,c} v_g^w - \tfrac{1}{6}\sum_{w=a,b,c}(v_p^w - v_n^w). \end{aligned} \tag{26}$$

Expanding the summation terms of (26), the ac current dynamics can be written in vector form as follows

$$L_t\dot{\mathbf{i}}_g^{abc} = -R_t\mathbf{i}_g^{abc} + \mathbf{Q}\left(\mathbf{v}_g^{abc} + \frac{1}{2}(\mathbf{v}_p^{abc} - \mathbf{v}_n^{abc})\right) \tag{27}$$

where $\mathbf{i}_g^{abc}$ and $\mathbf{v}_g^{abc}$ are similarly defined as the vectors in (25) and

$$\mathbf{Q} = \frac{1}{3}\begin{bmatrix} 2 & -1 & -1 \\ -1 & 2 & -1 \\ -1 & -1 & 2 \end{bmatrix}. \tag{28}$$

Proceeding as in (27), the circulating current dynamics (24) can also be written in vector form as follows

$$L_s\dot{\mathbf{i}}_{cir}^{abc} = -R_s\mathbf{i}_{cir}^{abc} + \frac{1}{2}\mathbf{Q}(\mathbf{v}_p^{abc} + \mathbf{v}_n^{abc}). \tag{29}$$

Then, the complete MMC current dynamics is obtained by combining (25), (27), and (29)

$$\frac{2}{3}L_s\dot{i}_{dc} = -\frac{2}{3}R_s i_{dc} - v_{dc} + 2\mathbf{p}^T\mathbf{v}_{sum}^{abc} \tag{30}$$

$$L_t\dot{\mathbf{i}}_g^{abc} = -R_t\mathbf{i}_g^{abc} + \mathbf{Q}(\mathbf{v}_g^{abc} - \mathbf{v}_{dif}^{abc}) \tag{31}$$

$$L_s\dot{\mathbf{i}}_{cir}^{abc} = -R_s\mathbf{i}_{cir}^{abc} + \mathbf{Q}\mathbf{v}_{sum}^{abc} \tag{32}$$

where

$$\mathbf{v}_{sum}^{abc} = \frac{1}{2}(\mathbf{v}_n^{abc} + \mathbf{v}_p^{abc}) \tag{33}$$

$$\mathbf{v}_{dif}^{abc} = \frac{1}{2}(\mathbf{v}_n^{abc} - \mathbf{v}_p^{abc}). \tag{34}$$

The positive and negative arm voltages can be recovered from the above auxiliary sum and difference voltages as follows

$$\mathbf{v}_p^{abc} = \mathbf{v}_{sum}^{abc} - \mathbf{v}_{dif}^{abc} \tag{35}$$

$$\mathbf{v}_n^{abc} = \mathbf{v}_{sum}^{abc} + \mathbf{v}_{dif}^{abc}. \tag{36}$$

The system (30)–(32) in the abc stationary reference frame can be transformed to the $o\alpha\beta$ stationary reference frame by using the Clarke transformation ($\mathbf{x}^{o\alpha\beta} = \mathbf{F}\mathbf{x}^{abc}$)

$$\mathbf{F} = \frac{2}{3}\begin{bmatrix} \frac{1}{\sqrt{2}} & \frac{1}{\sqrt{2}} & \frac{1}{\sqrt{2}} \\ 1 & -\frac{1}{2} & -\frac{1}{2} \\ 0 & -\frac{\sqrt{3}}{2} & \frac{\sqrt{3}}{2} \end{bmatrix}. \tag{37}$$

Applying the transformation (37) (i.e., $\mathbf{v}_{\text{sum}}^{\text{abc}} = \mathbf{F}^{-1}\mathbf{v}_{\text{sum}}^{o\alpha\beta}$) to (30) results in

$$\frac{2}{3}L_s\dot{i}_{\text{dc}} = -\frac{2}{3}R_s i_{\text{dc}} - v_{\text{dc}} + 2\mathbf{p}^T\mathbf{F}^{-1}\mathbf{v}_{\text{sum}}^{o\alpha\beta} \tag{38}$$

where $\mathbf{v}_{\text{sum}}^{o\alpha\beta} = [v_{\text{sum}}^{o}\ v_{\text{sum}}^{\alpha}\ v_{\text{sum}}^{\beta}]^T$ and $\mathbf{p}^T\mathbf{F}^{-1} = [\frac{1}{\sqrt{2}}\,0\,0]$. Then, it can be written

$$\frac{2}{3}L_s\dot{i}_{\text{dc}} = -\frac{2}{3}R_s i_{\text{dc}} - v_{\text{dc}} + \sqrt{2}v_{\text{sum}}^{o}. \tag{39}$$

In the same way, the transformation (37) can be applied to the ac current dynamics and the circulating current dynamics (31) and (32) obtaining

$$L_t\dot{\mathbf{i}}_g^{o\alpha\beta} = -R_t\mathbf{i}_g^{o\alpha\beta} + \mathbf{H}(\mathbf{v}_g^{o\alpha\beta} - \mathbf{v}_{\text{dif}}^{o\alpha\beta}) \tag{40}$$

and

$$L_s\dot{\mathbf{i}}_{\text{cir}}^{o\alpha\beta} = -R_s\mathbf{i}_{\text{cir}}^{o\alpha\beta} + \mathbf{H}\mathbf{v}_{\text{sum}}^{o\alpha\beta} \tag{41}$$

respectively, where

$$\mathbf{H} = \mathbf{FQF}^{-1} = \begin{bmatrix} 0 & 0 & 0 \\ 0 & 1 & 0 \\ 0 & 0 & 1 \end{bmatrix}. \tag{42}$$

3. Submodule capacitor voltages

The voltage dynamics of the submodule capacitors [see Fig. 1(a)] is given by

$$C^{\text{SM}}\dot{v}_{\text{Cp}}^{\text{SMjz}} = -\frac{v_{\text{Cp}}^{\text{SMjz}}}{R^{\text{SM}}} - s_p^{\text{jz}}i_p^z \tag{43}$$

$$C^{\text{SM}}\dot{v}_{\text{Cn}}^{\text{SMjz}} = -\frac{v_{\text{Cn}}^{\text{SMjz}}}{R^{\text{SM}}} - s_n^{\text{jz}}i_n^z \tag{44}$$

where s^j stands for the state (ON or OFF) of the jth submodule (i.e., $s^j = 1$ or $s^j = 0$, respectively), the subscript $j = \{1, \ldots, N\}$ represents the submodule index, and N is the number of submodules in each arm of the MMC. In this work, we assume equal parameters in each submodule, but individual resistances and capacitances can be considered by defining different values of $R^{\text{SM}j}$ and $C^{\text{SM}j}$ in (43) and (44). The equations (43) and (44) can be written in vector form as follows

$$C^{\text{SM}}\dot{\mathbf{v}}_{\text{Cp}}^{\text{SMz}} = -\frac{1}{R^{\text{SM}}}\mathbf{v}_{\text{Cp}}^{\text{SMz}} - \mathbf{s}_p^z\left(\frac{i_{\text{dc}}}{3} + \frac{i_g^z}{2} + i_{\text{cir}}^z\right) \tag{45}$$

$$C^{\text{SM}}\dot{\mathbf{v}}_{\text{Cn}}^{\text{SMz}} = -\frac{1}{R^{\text{SM}}}\mathbf{v}_{\text{Cn}}^{\text{SMz}} - \mathbf{s}_n^z\left(\frac{i_{\text{dc}}}{3} - \frac{i_g^z}{2} + i_{\text{cir}}^z\right) \tag{46}$$

where

$$\mathbf{v}_{\text{Cp}}^{\text{SMz}} = [v_{\text{Cp}}^{\text{SM1z}}\ \ v_{\text{Cp}}^{\text{SM2z}}\ \ \cdots\ \ v_{\text{Cp}}^{\text{SMNz}}]^T \in \Re^{N\times 1} \tag{47}$$

$$\mathbf{v}_{\text{Cn}}^{\text{SMz}} = [v_{\text{Cn}}^{\text{SM1z}}\ \ v_{\text{Cn}}^{\text{SM2z}}\ \ \cdots\ \ v_{\text{Cn}}^{\text{SMNz}}]^T \in \Re^{N\times 1} \tag{48}$$

$$\mathbf{s}_p^z = [s_p^{1z}\ \ s_p^{2z}\ \ \cdots\ \ s_p^{\text{Nz}}]^T \in \Re^{N\times 1} \tag{49}$$

$$\mathbf{s}_n^z = [s_n^{1z}\ \ s_n^{2z}\ \ \cdots\ \ s_n^{\text{Nz}}]^T \in \Re^{N\times 1} \tag{50}$$

and the arm currents i_p^z and i_n^z have been replaced by their expressions (9) and (10), respectively.

The output voltage of each submodule is given by

$$v_p^{\text{jz}} = s_p^{\text{jz}}v_{\text{Cp}}^{\text{SMjz}} - R_{\text{on}}i_p^z \tag{51}$$

$$v_n^{\text{jz}} = s_n^{\text{jz}}v_{\text{Cn}}^{\text{SMjz}} - R_{\text{on}}i_n^z \tag{52}$$

where R_{on} is the conduction (or on-state) resistance of the submodule switches. From (51) and (52), the total arm voltages are calculated as follows

$$v_p^z = \sum_{j=1}^{N} v_p^{\text{jz}} = (\mathbf{s}_p^z)^T\mathbf{v}_{\text{Cp}}^{\text{SMz}} - NR_{\text{on}}i_p^z \tag{53}$$

$$v_n^z = \sum_{j=1}^{N} v_n^{\text{jz}} = (\mathbf{s}_n^z)^T\mathbf{v}_{\text{Cn}}^{\text{SMz}} - NR_{\text{on}}i_n^z. \tag{54}$$

On the other hand, the sum of all submodule capacitor voltages in each arm is denoted by

$$v_{\text{Cp}}^{\text{armz}} = \sum_{j=1}^{N} v_{\text{Cp}}^{\text{SMjz}} = N\bar{v}_{\text{Cp}}^{\text{SMz}} \tag{55}$$

$$v_{\text{Cn}}^{\text{armz}} = \sum_{j=1}^{N} v_{\text{Cn}}^{\text{SMjz}} = N\bar{v}_{\text{Cn}}^{\text{SMz}} \tag{56}$$

where the superbar stands for an average value. If it is considered that the intra-arm voltage balancing achieves an even distribution of the submodule capacitor voltages in each arm, these voltages can be approximated by their average value, that is, $v_{\text{Cp}}^{\text{SMjz}} \cong \bar{v}_{\text{Cp}}^{\text{SMz}}$ and $v_{\text{Cn}}^{\text{SMjz}} \cong \bar{v}_{\text{Cn}}^{\text{SMz}}$. Therefore, the arm voltages (53) and (54) can be written as a function of the sum of all submodule capacitor voltages in each arm as follows

$$v_p^z = m_p^z v_{\text{Cp}}^{\text{armz}} - NR_{\text{on}}i_p^z \tag{57}$$

$$v_n^z = m_n^z v_{\text{Cn}}^{\text{armz}} - NR_{\text{on}}i_n^z \tag{58}$$

where m_n^z and m_p^z are the modulation (or insertion) indices defined as the ratio between the number of inserted submodules and the total number of submodules in the arm [13]

$$m_p^z = \frac{1}{N}\sum_{j=1}^{N} s_p^{\text{jz}} \tag{59}$$

$$m_n^z = \frac{1}{N}\sum_{j=1}^{N} s_n^{\text{jz}}. \tag{60}$$

4. MMC current control

Considering the decoupled current model (39)–(41), the currents i_{dc}, $\mathbf{i}_g$, and $\mathbf{i}_{cir}$ can be independently controlled by using the voltages v_{sum}^o, $\mathbf{v}_{dif}$, and $\mathbf{v}_{sum}$, respectively, which greatly facilitates the converter control. In the following, balanced ac grid conditions are considered, but the extension to unbalanced conditions can be found in [37,38]. This assumption is justified because we are studying an MMC model for eigenvalue analysis and electromechanical transient simulations (i.e., a positive-sequence model).

4.1. AC current control

The ac current dynamics (40) is analogous to the one of the traditional VSC. Therefore, conventional control strategies based on vector control in a synchronous reference frame can be used to control the ac current. A detailed description of this control is given in Appendix A.

4.2. Circulating current control

The circulating current $\mathbf{i}_{cir}$ is controlled via the voltage $\mathbf{v}_{sum}$. This control is implemented in the $\alpha\beta$ stationary reference frame, as described in the following steps.

4.2.1. Discrete state-space representation of the circulating current dynamics

From the definition of the circulating current given in Section 2.1 and considering (11), the zero-sequence component of this current is

null; therefore, the circulating current dynamics (41) is simplified to

$$\frac{1}{\Omega_B} L_s \dot{\mathbf{i}}_{\text{cir}}^{\alpha\beta} = -R_s \mathbf{i}_{\text{cir}}^{\alpha\beta} + \mathbf{v}_{\text{sum}}^{\alpha\beta} \tag{61}$$

where $\mathbf{i}_{\text{cir}}^{\alpha\beta} = [i_{\text{cir}}^{\alpha}\ i_{\text{cir}}^{\beta}]^T$ and $\mathbf{v}_{\text{sum}}^{\alpha\beta} = [v_{\text{sum}}^{\alpha}\ v_{\text{sum}}^{\beta}]^T$, with (61) written in per-unit values on the converter base, and Ω_B being the system angular frequency (in this work, $\Omega_B = 2\pi \times 50$ rad/s). The above system can be expressed in a state-space representation as follows

$$\dot{\mathbf{i}}_{\text{cir}}^{\alpha\beta} = \mathbf{A}_s \mathbf{i}_{\text{cir}}^{\alpha\beta} + \mathbf{B}_s \mathbf{v}_{\text{sum}}^{\alpha\beta} \tag{62}$$

where $\mathbf{A}_s = -\frac{R_s \Omega_B}{L_s}\mathbf{I}$ and $\mathbf{B}_s = \frac{\Omega_B}{L_s}\mathbf{I}$, and $\mathbf{I}$ is the 2×2 identity matrix. The continuous-time domain system (62) is discretized using the zero-order hold (ZOH) method and represented in the discrete-time domain resulting in

$$\mathbf{i}_{\text{cir}(k+1)}^{\alpha\beta} = \mathbf{G}_s \mathbf{i}_{\text{cirk}}^{\alpha\beta} + \mathbf{H}_s \mathbf{v}_{\text{sumk}}^{\alpha\beta}. \tag{63}$$

The matrices of the discrete system are calculated as $\mathbf{G}_s = e^{\mathbf{A}_s T_s}$ and $\mathbf{H}_s = \int_0^{T_s} e^{\mathbf{A}_s \tau} d\tau \mathbf{B}_s$, with T_s being the control sampling time [39].

4.2.2. Computational delay compensation

The computational time delay can be considered in the control design by defining an auxiliary control input $\mathbf{n}_{\text{sum}}^{\alpha\beta}$ as follows

$$\mathbf{v}_{\text{sum}(k+1)}^{\alpha\beta} = \mathbf{n}_{\text{sumk}}^{\alpha\beta}. \tag{64}$$

The variable $\mathbf{n}_{\text{sum}}^{\alpha\beta}$ is one-sample time behind the control signal $\mathbf{v}_{\text{sum}}^{\alpha\beta}$ and emphasizes the delay between the measurement process and the control signal update. In this way, the controller considers the computational delay, improving the tracking performance and avoiding stability problems.

4.2.3. Control specifications

As it will be explained in Section 5, the circulating current controller has to be able to: (i) control dc components, (ii) control fundamental-frequency positive- and negative-sequence components, and (iii) nullify undesired double-line-frequency (2ω) ripples. These requirements can be met as follows: first, a proportional-integral (PI) control is implemented to track the constant (or dc) components; second, a resonant control (with resonant frequency at ω) is added to guarantee a zero steady-state error in the tracking of fundamental-frequency references; third, a resonant control (with resonant frequency at 2ω) is included to nullify the double-line-frequency ripples. Additional resonant blocks can also be added to nullify higher frequency ripples in the circulating current. A procedure to extend the system model with these control elements is given below.

This approach of using proportional-integral-resonant (PIR) controls in the $\alpha\beta$ stationary reference frame allows to control both positive- and negative-sequence components of the circulating currents without steady-state error and only requires a frequency-locked loop to adjust the resonance frequency [40].

4.2.4. Extended model for the control design

The integral action of a PI controller $Q(s) = \frac{1}{s}E(s)$ can be implemented in the discrete-time domain as $q_{k+1} = q_k + T_s e_k$. In the case of the circulating current control, two integrators are required (one for the α-axis and another one for the β-axis), which can be written in vector form as follows

$$\mathbf{q}_{\text{cir}(k+1)} = \mathbf{q}_{\text{cirk}} + T_s \mathbf{e}_{\text{cirk}}^{\alpha\beta} \tag{65}$$

where $\mathbf{e}_{\text{cirk}}^{\alpha\beta} = \mathbf{i}_{\text{cirk}}^{\alpha\beta} - \mathbf{i}_{\text{cirk}}^{\star\alpha\beta}$ is the tracking error, and the superscript '$\star$' indicates a reference value. On the other hand, in the continuous-time domain, a resonant filter with resonant frequency at ω_r is given by

$$G_r(s) = \frac{H(s)}{E(s)} = \frac{s}{s^2 + \omega_r^2}. \tag{66}$$

Two transfer functions of the form (66) (one for each α–β component) can be discretized using the ZOH method and written in a state-space representation as

$$\mathbf{h}_{k+1}^{\omega_r} = \mathbf{A}^{\omega_r} \mathbf{h}_k^{\omega_r} + \mathbf{B}^{\omega_r} \mathbf{e}_{\text{cirk}}^{\alpha\beta} \tag{67}$$

where $\mathbf{h}_k^{\omega_r} \in \Re^{4\times 1}$ is the state vector of the resonant filters. Then, by combining the circulating current model (63), the computational delay model (64), the PI control integrators (65), and the resonant filters with resonant frequencies at ω and 2ω (67), the extended model is obtained as follows

$$\mathbf{w}_{c(k+1)} = \mathbf{A}_{\text{ce}} \mathbf{w}_{\text{ck}} + \mathbf{B}_{\text{ce}} \mathbf{n}_{\text{sumk}}^{\alpha\beta} - \mathbf{B}_{\text{ce}}^r \mathbf{i}_{\text{cirk}}^{\star\alpha\beta} \tag{68}$$

with state vector

$$\mathbf{w}_{\text{ck}} = [\mathbf{i}_{\text{cirk}}^{\alpha\beta}\ \ \mathbf{v}_{\text{sumk}}^{\alpha\beta}\ \ \mathbf{q}_{\text{cirk}}\ \ \mathbf{h}_k^{\omega}\ \ \mathbf{h}_k^{\omega 2}]^T \tag{69}$$

and matrices

$$\mathbf{A}_{\text{ce}} = \begin{bmatrix} \mathbf{G}_s & \mathbf{H}_s & \mathbf{0} & \mathbf{0} & \mathbf{0} \\ \mathbf{0} & \mathbf{0} & \mathbf{0} & \mathbf{0} & \mathbf{0} \\ T_s\mathbf{I} & \mathbf{0} & \mathbf{I} & \mathbf{0} & \mathbf{0} \\ \mathbf{B}^{\omega} & \mathbf{0} & \mathbf{0} & \mathbf{A}^{\omega} & \mathbf{0} \\ \mathbf{B}^{\omega 2} & \mathbf{0} & \mathbf{0} & \mathbf{0} & \mathbf{A}^{\omega 2} \end{bmatrix} \tag{70}$$

$$\mathbf{B}_{\text{ce}} = [\mathbf{0}\ \ \mathbf{I}\ \ \mathbf{0}\ \ \mathbf{0}\ \ \mathbf{0}]^T \tag{71}$$

$$\mathbf{B}_{\text{ce}}^r = [\mathbf{0}\ \ \mathbf{0}\ \ T_s\mathbf{I}\ \ \mathbf{B}^{\omega}\ \ \mathbf{B}^{\omega 2}]^T. \tag{72}$$

As it was previously stated, if additional resonant blocks need to be considered, they can be added by extending the matrices (70)–(72) (see [41]).

4.2.5. Control law

The control design is performed using a state-space approach, where the extended states (69) are fed back with the control law

$$\mathbf{n}_{\text{sumk}}^{\alpha\beta} = -\mathbf{K}\mathbf{w}_{\text{ck}}. \tag{73}$$

Substituting (73) into (68), the closed-loop system results in

$$\mathbf{w}_{c(k+1)} = (\mathbf{A}_{\text{ce}} - \mathbf{B}_{\text{ce}}\mathbf{K})\mathbf{w}_{\text{ck}} - \mathbf{B}_{\text{ce}}^r \mathbf{i}_{\text{cirk}}^{\star\alpha\beta}. \tag{74}$$

Then, the gain matrix $\mathbf{K}$ is designed so that the closed-loop matrix $(\mathbf{A}_{ce} - \mathbf{B}_{ce}\mathbf{K})$ has stable eigenvalues. To this end, linear techniques such as eigenvalue assignment, H-infinity control, or the linear quadratic regulator (LQR) method can be used. The last one is chosen in our work, where the matrix $\mathbf{K}$ is calculated so that the state-feedback law (73) minimizes the quadratic cost function $J = \sum_{k=0}^{\infty} \{\mathbf{w}_{\text{ck}}^T \mathbf{Q} \mathbf{w}_{\text{ck}} + (\mathbf{n}_{\text{sumk}}^{\alpha\beta})^T \mathbf{R} \mathbf{n}_{\text{sumk}}^{\alpha\beta}\}$. The matrices $\mathbf{Q}$ and $\mathbf{R}$ are the weighting matrices of the states $\mathbf{w}_c$ and the control inputs $\mathbf{n}_{\text{sum}}^{\alpha\beta}$, respectively. The solution of this problem is found by solving the associated algebraic Riccati equation (see [39,42] for further details). In practice, the weighting matrices are usually diagonal. The relative values of the diagonal elements of $\mathbf{Q}$ determine the relative importance attached to certain states. For example, a large value in the diagonal element $q_{\{i,i\}}$ will penalize the transient deviation of the ith state (i.e., a lower tracking error). Similarly, a large value in the diagonal of $\mathbf{R}$ will penalize the action of the corresponding control input (i.e., a smaller control effort). As a general guideline, the relative values of the design matrices $\mathbf{Q}$ and $\mathbf{R}$ must be selected as a trade-off between the desired tracking performance and the magnitude of the control inputs. If a particular control input is excessively saturated, it can be more heavily weighed to reduce its magnitude. Since the pair $(\mathbf{A}_{ce}, \mathbf{B}_{ce})$ is controllable (i.e., its controllability matrix has full rank), and by choosing $\mathbf{Q}$ and $\mathbf{R}$ positive semi-definite and definite, respectively, the LQR method guarantees that the closed-loop matrix will have stable eigenvalues [39].

4.3. DC current control

The dc current dynamics (39) is a first-order decoupled system that can be regulated via v_{sum}^o, using a PI controller with a feedforward term to compensate the dc-bus voltage variations (see control system block

diagrams in following sections).

4.4. Active and reactive power references

The ac current references are provided by outer control loops. The reactive current (or power) reference can be set either to a desired value (e.g., unity power factor condition) or to regulate the ac-bus voltage. On the other hand, the active component reference can be set either to a fixed value (P-Q operation mode) or to regulate the dc-bus voltage (v_{dc}-Q operation mode). Depending on the application, the dc-bus voltage controller is implemented using specific schemes such as droop control and voltage margin control, among others. A detailed description of these control schemes is given in [43].

As a general rule in cascade structures, the outer controls are designed to have a bandwidth ten times slower than the inner current controls. In this way, any adverse interaction between outer and inner control loops is avoided.

4.5. Modulation technique

Once the modulation indices are calculated from the inner current control loops, a modulation technique, such as nearest level control (NLC), pulse-width modulation, or selective harmonic elimination, can be used to obtain the drive signals of the submodule switches. The NLC, which is a staircase-type modulation, is chosen in this work because it is preferred for high-voltage and high-power applications (i.e., MMCs with high number of submodules). Among its advantages are the low switching losses, less computational effort, and simple implementation [2]. A third-order harmonic is added to the modulation signal of the difference voltage $\mathbf{v}_{dif}$ (i.e., to the ac current control) to maximize the use of the capacitor voltages [44].

5. Balancing of the arm energies

The MMC control system has to control both the converter currents and the submodule capacitor voltages. The latter is performed in two stages: in a first stage (called intra-arm balancing) the capacitor voltages inside each arm are equally distributed using the sorting (or module selection) method (see [44]); in a second stage, outer control loops balance the arm energies (inter-arm balancing) and regulate the total energy stored in the converter capacitors [36]. The inter-arm balancing can be divided into the horizontal balancing, which equalizes the energy of the three legs (inter-leg balancing), and the vertical balancing, which equalizes the energy between the positive and negative arms of each leg (intra-leg balancing). These outer control loops balance the arm energies acting on the inner current control loops, as it will be described below.

5.1. Voltage and current components

Under normal operating conditions, the voltage and current phasors on the ac side have only positive-sequence components, and they are represented by $\vec{v}_g^{\,abc} = V_g e^{j(\omega t+\theta_g)}$, $\vec{v}_{dif}^{\,abc} = V_{dif} e^{j(\omega t+\theta_{dif})}$, and $\vec{i}_g^{\,abc} = I_g e^{j(\omega t+\varphi_g)}$, where V_g, V_{dif}, and I_g are the magnitudes of the ac voltage, the difference voltage, and the ac current, respectively, whereas the angles θ_g, θ_{dif}, and φ_g are their respective phases. The a-phase of these signals is expressed as: $v_g^a = V_g \sin(\omega t + \theta_g)$, $v_{dif}^a = V_{dif} \sin(\omega t + \theta_{dif})$, and $i_g^a = I_g \sin(\omega t + \varphi_g)$. On the other hand, the sum voltage has only a dc component (i.e., $v_{sum}^z = v_{sum}^{dc}$) [14], and the circulating current is nullified by its controller to reduce the converter steady-state losses. However, the circulating current can be transiently managed to perform the inter-arm balancing [35]. With this aim, both the dc components and the fundamental-frequency positive- and negative-sequence components of the circulating current have to be controlled. The a-phase of this current is expressed as

$$i_{cir}^a = I_{cir}^+ \sin(\omega t + \varphi_{cir}^+) + I_{cir}^- \sin(-\omega t + \varphi_{cir}^-) + i_{cir}^{a\,dc}$$

where I_{cir}^+ and I_{cir}^- are the magnitudes of the positive- and negative-sequence components, φ_{cir}^+ and φ_{cir}^- are their phases, and $i_{cir}^{a\,dc}$ is the dc component.

The use of the circulating current to balance the arm energies is advantageous because this current is independent (or decoupled) from the ac and dc output currents; therefore, the energy balancing is internally performed by the converter controller and, from an input-output point of view, it does not disturb the terminal behavior of the MMC [36]. This fact will be considered in the reduced MMC model in Section 6.

5.2. Mean-value dynamics of the arm energies

The time derivative of the arm energies is given by

$$\dot{e}_p^z = p_p^z \tag{75}$$

$$\dot{e}_n^z = p_n^z \tag{76}$$

where p_p^z and p_n^z are the positive and negative arm powers; neglecting the arm losses, they can be calculated as follows

$$p_p^z = v_p^z i_p^z = (v_{sum}^z - v_{dif}^z)\left(\frac{i_{dc}}{3} + \frac{i_g^z}{2} + i_{cir}^z\right) \tag{77}$$

$$p_n^z = v_n^z i_n^z = (v_{sum}^z + v_{dif}^z)\left(\frac{i_{dc}}{3} - \frac{i_g^z}{2} + i_{cir}^z\right) \tag{78}$$

where (9), (10) and (35), (36) have been used. To simplify the analysis of the horizontal and vertical balancing, the sum and difference energies $e_{sum}^z = e_n^z + e_p^z$ and $e_{dif}^z = e_n^z - e_p^z$ are defined. Therefore, adding and subtracting (75) and (76), and considering (77) and (78), result in

$$\dot{e}_{sum}^z = \frac{2}{3} v_{sum}^z i_{dc} - v_{dif}^z i_g^z + 2 v_{sum}^z i_{cir}^z \tag{79}$$

$$\dot{e}_{dif}^z = \frac{2}{3} v_{dif}^z i_{dc} - v_{sum}^z i_g^z + 2 v_{dif}^z i_{cir}^z. \tag{80}$$

The dynamics of the sum and difference energies (79) and (80) can be written in vector form and in the *abc* reference frame, as follows

$$\dot{\mathbf{e}}_{sum}^{abc} = \frac{2}{3}\mathbf{v}_{sum}^{abc} i_{dc} - \mathbf{v}_{dif}^{abc} \circ \mathbf{i}_g^{abc} + 2\mathbf{v}_{sum}^{abc} \circ \mathbf{i}_{cir}^{abc} \tag{81}$$

$$\dot{\mathbf{e}}_{dif}^{abc} = \frac{2}{3}\mathbf{v}_{dif}^{abc} i_{dc} - \mathbf{v}_{sum}^{abc} \circ \mathbf{i}_g^{abc} + 2\mathbf{v}_{dif}^{abc} \circ \mathbf{i}_{cir}^{abc} \tag{82}$$

where $\circ$ stands for the element-by-element multiplication. Transforming (81) to the $o\alpha\beta$ reference frame and considering the voltage and current components described in the previous subsection, the components of the vector $\dot{\mathbf{e}}_{sum}^{o\alpha\beta}$ give

$$\dot{e}_{sum}^o = \frac{2\sqrt{2}}{3} v_{sum}^{dc} i_{dc} - \frac{1}{\sqrt{2}} V_{dif} I_g \cos(\varphi_g - \theta_{dif}) \tag{83}$$

$$\begin{aligned}\dot{e}_{sum}^\alpha = {} & 2v_{sum}^{dc} i_{cir}^{\alpha\,dc} + 2v_{sum}^{dc} I_{cir}^+ \sin(\varphi_{cir}^+ + \omega t) + \\ & 2v_{sum}^{dc} I_{cir}^- \sin(\varphi_{cir}^- - \omega t) + \tfrac{1}{2} V_{dif} I_g \cos(\varphi_g + \theta_{dif} + 2\omega t)\end{aligned} \tag{84}$$

$$\begin{aligned}\dot{e}_{sum}^\beta = {} & 2v_{sum}^{dc} i_{cir}^{\beta\,dc} + 2v_{sum}^{dc} I_{cir}^+ \cos(\varphi_{cir}^+ + \omega t) + \\ & 2v_{sum}^{dc} I_{cir}^- \cos(\varphi_{cir}^- - \omega t) + \tfrac{1}{2} V_{dif} I_g \sin(\varphi_g + \theta_{dif} + 2\omega t).\end{aligned} \tag{85}$$

In (83)–(85), there are oscillating terms with sinusoidal shape (i.e., alternating powers with zero mean value) that introduce ripples in the arm energies, and other constant terms (i.e., non-alternating powers with non-zero mean value) that can be used to control the energy mean value. Because the inter-arm balancing is focused on regulating the mean value of the arm energies, only the non-alternating power terms need to be considered; therefore, (83)–(85) are reduced to

$$\dot{\bar{e}}^{o}_{\text{sum}} = \frac{2\sqrt{2}}{3} v^{\text{dc}}_{\text{sum}} i_{\text{dc}} - \frac{V_{\text{dif}} I_g \cos(\varphi_g - \theta_{\text{dif}})}{\sqrt{2}} \tag{86}$$

$$\dot{\bar{e}}^{\alpha}_{\text{sum}} = 2 v^{\text{dc}}_{\text{sum}} i^{\alpha\,\text{dc}}_{\text{cir}} \tag{87}$$

$$\dot{\bar{e}}^{\beta}_{\text{sum}} = 2 v^{\text{dc}}_{\text{sum}} i^{\beta\,\text{dc}}_{\text{cir}}. \tag{88}$$

Proceeding in a similar way, (82) is transformed to the $o\alpha\beta$ reference frame, and the mean-value dynamics of the difference energies is described by

$$\dot{\bar{e}}^{o}_{\text{dif}} = \sqrt{2} V_{\text{dif}} I^{+}_{\text{cir}} \cos(\varphi^{+}_{\text{cir}} - \theta_{\text{dif}}) \tag{89}$$

$$\dot{\bar{e}}^{\alpha}_{\text{dif}} = -V_{\text{dif}} I^{-}_{\text{cir}} \cos(\varphi^{-}_{\text{cir}} + \theta_{\text{dif}}) \tag{90}$$

$$\dot{\bar{e}}^{\beta}_{\text{dif}} = -V_{\text{dif}} I^{-}_{\text{cir}} \sin(\varphi^{-}_{\text{cir}} + \theta_{\text{dif}}). \tag{91}$$

The different energy components can be controlled by using certain converter currents as shown in (86)–(88) and (89)–(91). To obtain the references of these currents in the $o\alpha\beta$ reference frame, the above equations are converted from Polar to Cartesian coordinates.

In a generic phasor $\vec{x} = Xe^{j(\omega t+\phi)}$, the magnitude X and the phase ϕ are related to the α–β components as follows

$$\vec{x} = X\cos(\omega t + \phi) + j\,\text{X}\sin(\omega t + \phi) = x^{\beta} + jx^{\alpha}. \tag{92}$$

For example, in the case of the ac current, it is verified $i^{\alpha}_{g} = I_g \sin(\omega t + \varphi_g)$ and $i^{\beta}_{g} = I_g \cos(\omega t + \varphi_g)$, whereas the positive- and negative-sequence components of the circulating current are given by $i^{\alpha\,\pm}_{\text{cir}} = I^{\pm}_{\text{cir}} \sin(\pm\,\omega t + \varphi^{\pm}_{\text{cir}})$ and $i^{\beta\,\pm}_{\text{cir}} = I^{\pm}_{\text{cir}} \cos(\pm\,\omega t + \varphi^{\pm}_{\text{cir}})$. Then, (86)–(88) and (89)–(91) are converted to Cartesian coordinates using (92), which results in

$$\dot{\bar{e}}^{o}_{\text{sum}} = \frac{2\sqrt{2}}{3} v^{\text{dc}}_{\text{sum}} i_{\text{dc}} - \frac{v^{\alpha}_{\text{dif}} i^{\alpha}_{g} + v^{\beta}_{\text{dif}} i^{\beta}_{g}}{\sqrt{2}} \triangleq u^{o}_{\text{sum}} \tag{93}$$

$$\dot{\bar{e}}^{\alpha}_{\text{sum}} = 2 v^{\text{dc}}_{\text{sum}} i^{\alpha\,\text{dc}}_{\text{cir}} \triangleq u^{\alpha}_{\text{sum}} \tag{94}$$

$$\dot{\bar{e}}^{\beta}_{\text{sum}} = 2 v^{\text{dc}}_{\text{sum}} i^{\beta\,\text{dc}}_{\text{cir}} \triangleq u^{\beta}_{\text{sum}} \tag{95}$$

and

$$\dot{\bar{e}}^{o}_{\text{dif}} = \sqrt{2}\,(v^{\alpha}_{\text{dif}} i^{\alpha+}_{\text{cir}} + v^{\beta}_{\text{dif}} i^{\beta+}_{\text{cir}}) \triangleq u^{o}_{\text{dif}} \tag{96}$$

$$\dot{\bar{e}}^{\alpha}_{\text{dif}} = v^{\alpha}_{\text{dif}} i^{\alpha-}_{\text{cir}} - v^{\beta}_{\text{dif}} i^{\beta-}_{\text{cir}} \triangleq u^{\alpha}_{\text{dif}} \tag{97}$$

$$\dot{\bar{e}}^{\beta}_{\text{dif}} = -v^{\alpha}_{\text{dif}} i^{\beta-}_{\text{cir}} - v^{\beta}_{\text{dif}} i^{\alpha-}_{\text{cir}} \triangleq u^{\beta}_{\text{dif}}. \tag{98}$$

5.3. Total energy control and horizontal balancing

The total converter energy (i.e., the sum of all the arm energies) is regulated controlling the energy $\bar{e}^{o}_{\text{sum}}$, which is proportional to the total energy ($e_C = \frac{3}{\sqrt{2}} e^{o}_{\text{sum}}$). This is achieved by managing the power flow between the ac and dc sides. Depending on the MMC operation mode [9], this can be done using either the dc power $v^{\text{dc}}_{\text{sum}} i_{\text{dc}}$ or the ac power $v^{\alpha}_{\text{dif}} i^{\alpha}_{g} + v^{\beta}_{\text{dif}} i^{\beta}_{g}$ [see (93)].

On the other hand, the horizontal balancing is performed nullifying the energies $\bar{e}^{\alpha}_{\text{sum}}$ and $\bar{e}^{\beta}_{\text{sum}}$, which are controlled via the dc components $i^{\alpha\,\text{dc}}_{\text{cir}}$ and $i^{\beta\,\text{dc}}_{\text{cir}}$ of the circulating current [see (94) and (95)]. The dynamics of the sum energies are transformed to first-order systems of the form $\dot{\bar{e}}_{\text{sum}} = u_{\text{sum}}$ by defining the auxiliary control inputs u^{o}_{sum}, u^{α}_{sum} and u^{β}_{sum} [see (93)–(95)]. Then, PI controllers are designed to regulate the energies $\bar{e}_{\text{sum}}$ to the desired value. Finally, the current references to achieve the horizontal balancing are calculated from (94) and (95) as follows

$$i^{\star\alpha\,\text{dc}}_{\text{cir}} = \frac{u^{\alpha}_{\text{sum}}}{2 v^{\text{dc}}_{\text{sum}}} \tag{99}$$

$$i^{\star\beta\,\text{dc}}_{\text{cir}} = \frac{u^{\beta}_{\text{sum}}}{2 v^{\text{dc}}_{\text{sum}}} \tag{100}$$

where the auxiliary control inputs u^{α}_{sum} and u^{β}_{sum} are obtained from the mentioned PI controllers.

5.4. Vertical balancing

The vertical balancing is performed nullifying the energies $\bar{e}_{\text{dif}}$, which are controlled using the fundamental-frequency positive- and negative-sequence components $i^{\alpha+}_{\text{cir}}$, $i^{\beta+}_{\text{cir}}$, $i^{\alpha-}_{\text{cir}}$, and $i^{\beta-}_{\text{cir}}$ of the circulating current [see (96)–(98)]. Similar to the previous subsection, the auxiliary control inputs u^{o}_{dif}, u^{α}_{dif} and u^{β}_{dif} are defined to simplify the control design and to obtain decoupled first-order systems of the form $\dot{\bar{e}}_{\text{dif}} = u_{\text{dif}}$.

Because three energies need to be controlled (i.e., $\bar{e}^{o}_{\text{dif}}$, $\bar{e}^{\alpha}_{\text{dif}}$, and $\bar{e}^{\beta}_{\text{dif}}$), and there are four circulating current components to be chosen, an additional constraint is introduced to minimize the required apparent power [36]. This can be achieved by stating that the current $\mathbf{i}^{+}_{\text{cir}}$ is in-phase with the voltage $\mathbf{v}_{dif}$; that is, by zeroing the following reactive power

$$q_{\text{cir}} = v^{\alpha}_{\text{dif}} i^{\beta+}_{\text{cir}} - v^{\beta}_{\text{dif}} i^{\alpha+}_{\text{cir}} = 0. \tag{101}$$

Finally, the circulating current references to achieve the vertical balancing are calculated from (96)–(98) and (101) as follows

$$\begin{bmatrix} i^{\star\alpha+}_{\text{cir}} \\ i^{\star\beta+}_{\text{cir}} \\ i^{\star\alpha-}_{\text{cir}} \\ i^{\star\beta-}_{\text{cir}} \end{bmatrix} = \begin{bmatrix} v^{\alpha}_{\text{dif}} & v^{\beta}_{\text{dif}} & 0 & 0 \\ 0 & 0 & v^{\alpha}_{\text{dif}} & -v^{\beta}_{\text{dif}} \\ 0 & 0 & -v^{\beta}_{\text{dif}} & -v^{\alpha}_{\text{dif}} \\ -v^{\beta}_{\text{dif}} & v^{\alpha}_{\text{dif}} & 0 & 0 \end{bmatrix}^{-1} \begin{bmatrix} \frac{u^{o}_{\text{dif}}}{\sqrt{2}} \\ u^{\alpha}_{\text{dif}} \\ u^{\beta}_{\text{dif}} \\ 0 \end{bmatrix}. \tag{102}$$

A schematic block diagram of the complete MMC control system is shown in Fig. 2.

6. Reduced MMC model

6.1. Equivalent dynamics of all submodule capacitors

To reduce the order of the MMC model, it is assumed that the intra-arm balancing method achieves an even distribution of the submodule voltages in each arm. In this way, the individual submodule voltages do not need to be represented. Therefore, adding the voltage equation (43) for all the submodules results in

$$\frac{C^{\text{SM}}}{N} \dot{v}^{\text{arm}z}_{\text{Cp}} = -\frac{v^{\text{arm}z}_{\text{Cp}}}{R^{\text{SM}} N} - m^{z}_{p} i^{z}_{p} \tag{103}$$

where (55) and (59) have been used. Proceeding in a similar way with the voltage equation (44) and considering (9) and (10), we obtain

$$\frac{C^{\text{SM}}}{N} \dot{v}^{\text{arm}z}_{\text{Cp}} = -\frac{v^{\text{arm}z}_{\text{Cp}}}{R^{\text{SM}} N} - m^{z}_{p}\left(\frac{i_{\text{dc}}}{3} + \frac{i^{z}_{g}}{2} + i^{z}_{\text{cir}}\right) \tag{104}$$

$$\frac{C^{\text{SM}}}{N} \dot{v}^{\text{arm}z}_{\text{Cn}} = -\frac{v^{\text{arm}z}_{\text{Cn}}}{R^{\text{SM}} N} - m^{z}_{n}\left(\frac{i_{\text{dc}}}{3} - \frac{i^{z}_{g}}{2} + i^{z}_{\text{cir}}\right). \tag{105}$$

The equations (104) and (105) represent the voltage dynamics of the six arms modeled with an equivalent capacitor per arm. This reduces the MMC model to an eleventh-order model with five converter currents (i^{α}_{g}, i^{β}_{g}, i^{α}_{cir}, i^{β}_{cir}, and i_{dc}) and six arm voltages ($v^{\text{arm}a}_{\text{Cp}}$, $v^{\text{arm}b}_{\text{Cp}}$, $v^{\text{arm}c}_{\text{Cp}}$, $v^{\text{arm}a}_{\text{Cn}}$, $v^{\text{arm}b}_{\text{Cn}}$, and $v^{\text{arm}c}_{\text{Cn}}$) as state variables.

In the MMC, the ac output current passes through the submodule capacitors; therefore, the alternating arm currents cause ripples in the six arm voltages during normal steady-state operation. This is a drawback in power system stability studies where a constant equilibrium point is required both to initialize the states in time-domain simulations and to perform small-signal analysis. To overcome this problem, the

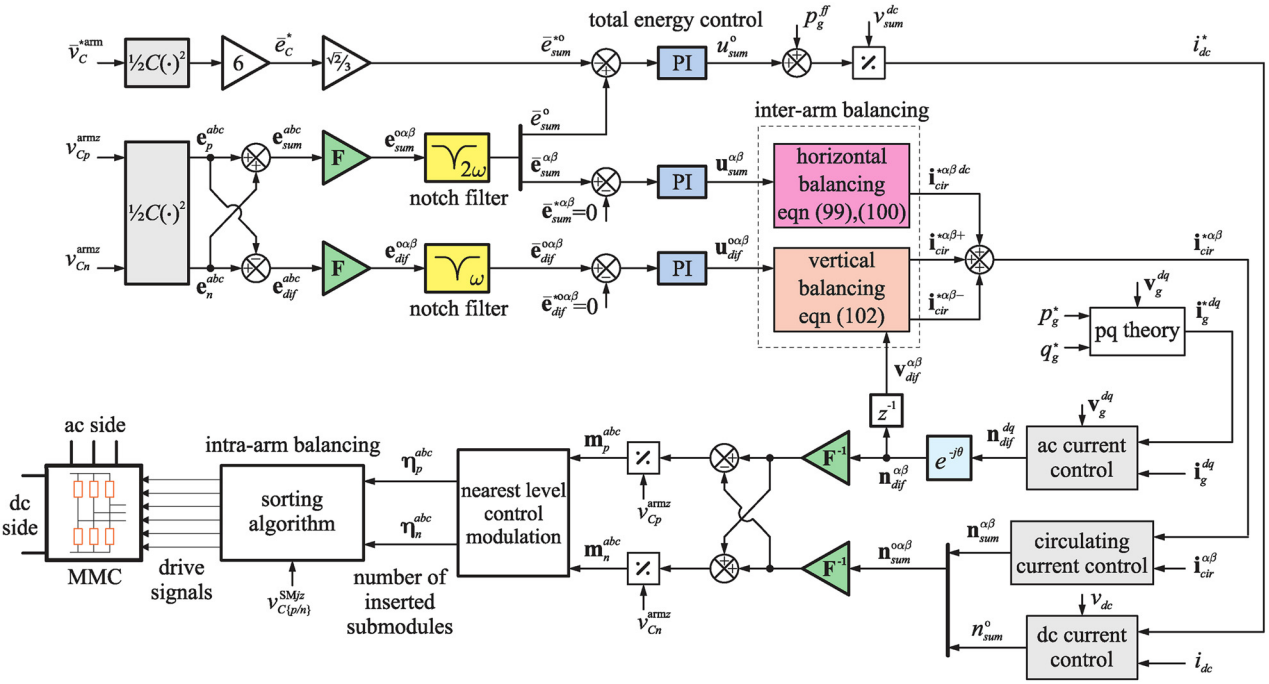

Fig. 2. Overview of the MMC control strategy used in the detailed model. Reference signals are filtered to avoid high frequency noise, and they are also limited to their maximum values (not shown for the sake of clarity).

MMC model can be further reduced by assuming that the inter-arm balancing method balances the six arm voltages, as described in Section 5. This allows to combine the voltage dynamics of the six arms in a single equivalent capacitor that represents the capacitive energy of all submodule capacitors. With this purpose, the voltage dynamics of each converter leg is firstly obtained by adding (104) and (105) (i.e., assuming $v_C^z = v_{\mathrm{Cp}}^{\mathrm{armz}} = v_{\mathrm{Cn}}^{\mathrm{armz}}$)

$$\frac{2C^{\mathrm{SM}}}{N}\dot{v}_C^z = -\frac{2v_C^z}{R^{\mathrm{SM}}N} - \frac{2}{3}m_{\mathrm{sum}}^z i_{\mathrm{dc}} + m_{\mathrm{dif}}^z i_g^z \tag{106}$$

where

$$m_{\mathrm{sum}}^z = \frac{1}{2}(m_n^z + m_p^z) \tag{107}$$

$$m_{\mathrm{dif}}^z = \frac{1}{2}(m_n^z - m_p^z). \tag{108}$$

As explained in Section 5, the circulating current is only transiently used to balance the arm energies, and then it is nullified by the circulating current control. Therefore, in (106), it has also been assumed that the circulating current is zero (i.e., $i_{\mathrm{cir}}^z = 0$). Finally, the total voltage dynamics is obtained by adding (106) for the three legs $z = \{a, b, c\}$ (i.e., assuming $v_C = v_C^z$)

$$C^{\mathrm{eq}}\dot{v}_C = -\frac{v_C}{R^{\mathrm{eq}}} - \sqrt{2}\,m_{\mathrm{sum}}^o i_{\mathrm{dc}} + (\mathbf{m}_{\mathrm{dif}}^{\mathrm{abc}})^T \mathbf{i}_g^{\mathrm{abc}} \tag{109}$$

where $C^{\mathrm{eq}} = \frac{6C^{\mathrm{SM}}}{N}$ and $R^{\mathrm{eq}} = \frac{R^{\mathrm{SM}}N}{6}$ are the equivalent capacitance and resistance, respectively, and $\mathbf{m}_{\mathrm{dif}}^{\mathrm{abc}} = [m_{\mathrm{dif}}^a\ m_{\mathrm{dif}}^b\ m_{\mathrm{dif}}^c]^T$. The capacitor time constant (i.e., the converter capacitive energy per volt-ampere) is given by $\tau_C = \frac{1}{2}C_{\mathrm{eq}}v_C^2/S_B$, where S_B is the rated power of the MMC.

6.2. Dynamics of the DC and AC currents

Assuming $R_{on} = 0$ and considering $v_C = v_{\mathrm{Cp}}^{\mathrm{armz}} = v_{\mathrm{Cn}}^{\mathrm{armz}}$, the arm voltages (57) and (58) are reduced to

$$v_p^z = m_p^z v_C \tag{110}$$

$$v_n^z = m_n^z v_C \tag{111}$$

and the following expressions are found using (107) and (108)

$$\mathbf{v}_{\mathrm{sum}}^{\mathrm{abc}} = \mathbf{m}_{\mathrm{sum}}^{\mathrm{abc}} v_C \tag{112}$$

$$\mathbf{v}_{\mathrm{dif}}^{\mathrm{abc}} = \mathbf{m}_{\mathrm{dif}}^{\mathrm{abc}} v_C. \tag{113}$$

Then, the dynamics of the dc and ac currents are obtained by substituting (112) and (113) into (30) and (31), respectively, which results in

$$\frac{2}{3}L_s\dot{i}_{\mathrm{dc}} = -\frac{2}{3}R_s i_{\mathrm{dc}} - v_{\mathrm{dc}} + \sqrt{2}\,m_{\mathrm{sum}}^o v_C \tag{114}$$

$$L_t\dot{\mathbf{i}}_g^{\mathrm{abc}} = -R_t\mathbf{i}_g^{\mathrm{abc}} + \mathbf{Q}(\mathbf{v}_g^{\mathrm{abc}} - \mathbf{m}_{\mathrm{dif}}^{\mathrm{abc}} v_C). \tag{115}$$

6.3. Transformation to DQ coordinates

In electromechanical transient simulations, to obtain constant values in steady state, the models are represented in *dq* coordinates using the Park transformation. This is achieved by transforming the variables from *abc* to *αβ* coordinates, and then from *αβ* to *dq* coordinates. To convert from the *αβ* stationary reference frame to the *dq* synchronous reference frame, the following Park transformation $\mathbf{f}^{\mathrm{dq}} = \mathbf{P}(\theta)\mathbf{f}^{\alpha\beta}$ is used

$$\mathbf{P}(\theta) = \begin{bmatrix} \cos\theta & -\sin\theta \\ \sin\theta & \cos\theta \end{bmatrix}. \tag{116}$$

Then, a fourth-order model of the MMC (with state variables: the output currents i_g^d, i_g^q, and i_{dc}, and the equivalent capacitor voltage v_C) is obtained by writing the current and voltage dynamics (114), (115), and (109) in *dq* coordinates, as follows

$$\frac{2}{3}L_s\dot{i}_{\mathrm{dc}} = -\frac{2}{3}R_s i_{\mathrm{dc}} - v_{\mathrm{dc}} + \widetilde{m}_{\mathrm{sum}}^o v_C \tag{117}$$

$$L_t\dot{i}_g^d = -R_t i_g^d - \omega L_t i_g^q + v_g^d - m_{\mathrm{dif}}^d v_C \tag{118}$$

$$L_t\dot{i}_g^q = -R_t i_g^q + \omega L_t i_g^d + v_g^q - m_{\mathrm{dif}}^q v_C \tag{119}$$

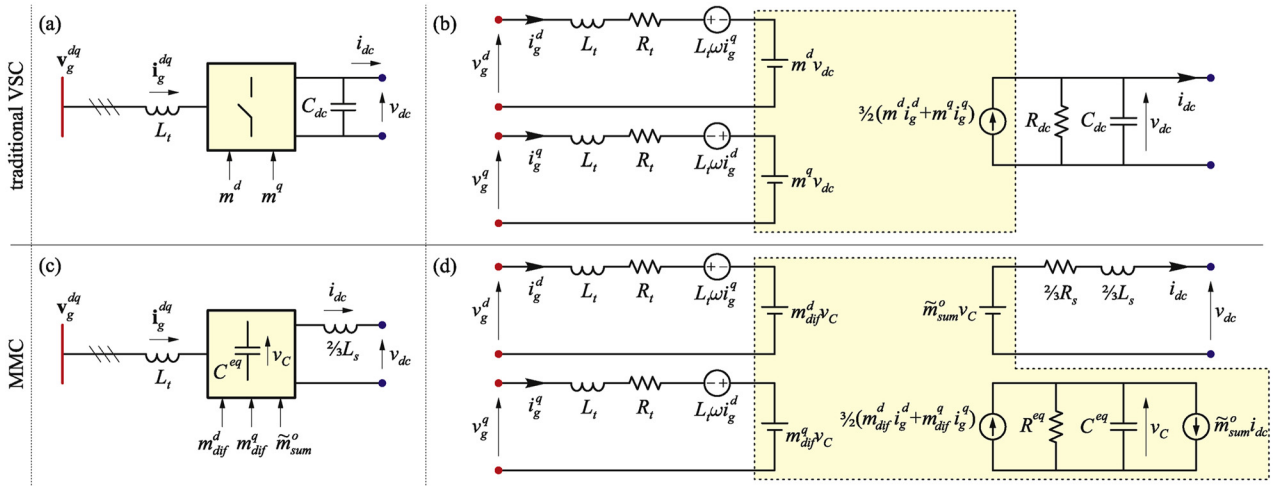

Fig. 3. Models of the ac/dc converter stations for transient stability studies. (a and b) Configuration and equivalent electrical circuit of the traditional VSC. (c and d) Configuration and equivalent electrical circuit of the MMC.

$$C^{\text{eq}}\dot{v}_C = -\frac{v_C}{R^{\text{eq}}} - \widetilde{m}^o_{\text{sum}} i_{\text{dc}} + \frac{3}{2}(m^d_{\text{dif}} i^d_g + m^q_{\text{dif}} i^q_g) \tag{120}$$

where $\widetilde{m}^o_{\text{sum}} = \sqrt{2}\, m^o_{\text{sum}}$. The resulting nonlinear model (117)–(120) can be linearized for small-signal (modal) analysis. Note that the model equations (117) and (120) explicitly reflect the effect of the zero-sequence modulation index on the dc-side behavior. If the conduction resistance is considered, the corrected values $R_s^{\text{corr}} = R_s + NR_{\text{on}}$ and $R_t^{\text{corr}} = R_e + \frac{1}{2}R_s^{\text{corr}}$ have to be used.

6.4. Comparison between the traditional VSC and the MMC

Electrical circuits representing the traditional VSC model [45] and the MMC model (117)–(120) are shown in Fig. 3. Both converters have a similar representation on the ac side, but a different one on the dc side. The MMC directly controls the dc current through the inductance $2/3L_s$ [see Fig. 3(d)]; thus, it has a current-source characteristic on the dc side (inductive ending) [9]. On the other hand, the traditional VSC configuration, due to the concentrated dc capacitor C_{dc}, directly controls the dc-bus voltage and has a voltage-source characteristic on the dc side (capacitive ending). The traditional VSC model does not reflect the dc-side behavior of the MMC because the MMC capacitors are not directly coupled to the dc bus, like in the case of the traditional VSC [20]. The operating characteristics of the MMC are better represented by modeling the total converter voltage v_C (i.e., the sum of all submodule capacitor voltages) and the dc-bus voltage v_{dc} as independent variables [32] [see MMC representation in Fig. 3(d)].

7. Control of the reduced MMC model

Power system simulations involve a large number of continuous-time ordinary differential equations, which are then solved by the Euler and trapezoidal methods. Therefore, in order to integrate the reduced MMC model to these simulations, its control system has to be also implemented in the continuous-time domain. On the other hand, as performed in Section 4 for the control design, it is convenient to convert the system (117)–(120) to per-unit values on the converter base. Thus, the control parameters are independent of the converter rated power, simplifying the tuning and implementation of the controls in studies with multiple MMCs.

First, the dc and ac current dynamics (117)–(119) are transformed to three decoupled first-order linear systems by defining the following auxiliary control inputs

$$w^o_{\text{sum}} \triangleq -v_{\text{dc}} + \widetilde{m}^o_{\text{sum}} v_C \tag{121}$$

$$w^d_{\text{dif}} \triangleq -\omega L_t i^q_g + v^d_g - m^d_{\text{dif}} v_C \tag{122}$$

$$w^q_{\text{dif}} \triangleq \omega L_t i^d_g + v^q_g - m^q_{\text{dif}} v_C. \tag{123}$$

The resulting systems, of the form $L\dot{i} = -\text{R i} + w$, are regulated using PI controllers, and then the modulation indices $\widetilde{m}^o_{\text{sum}}$, m^d_{dif}, and m^q_{dif} are calculated from (121)–(123). The current references for these systems are obtained from outer control loops, as previously explained in Section 4.4. Fig. 4 shows a block diagram of the control system for the reduced model, where droop controls are chosen to regulate the ac- and dc-bus voltages, and an energy-based control is used to regulate the total converter energy $e_C = \frac{1}{2}C^{\text{eq}}v_C^2$ [15]. As recommended in [1], a transient droop compensation is included to transiently reduce the control gain and to avoid exciting the transmission line modes.

8. Performance assessment

The tests are performed using the 1000-MW MMC with 400 submodules per arm of the France-Spain electrical interconnection (INELFE) project (see converter parameters in [21]).

8.1. MMC operation and control system performance

A test is carried out to verify the performance of both the current

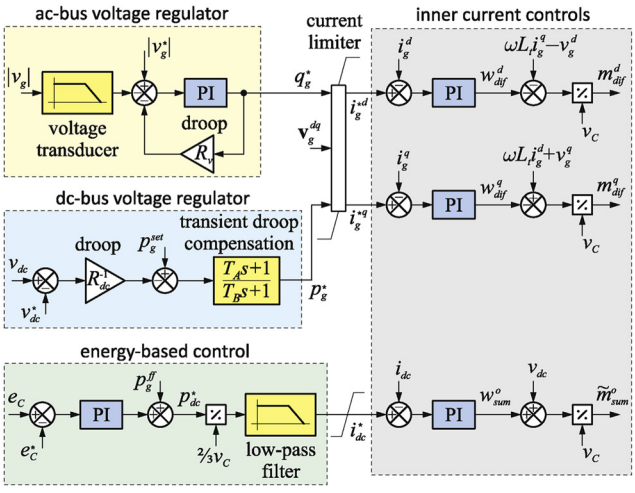

Fig. 4. Control system for the reduced MMC model including both the inner and the outer control loops.

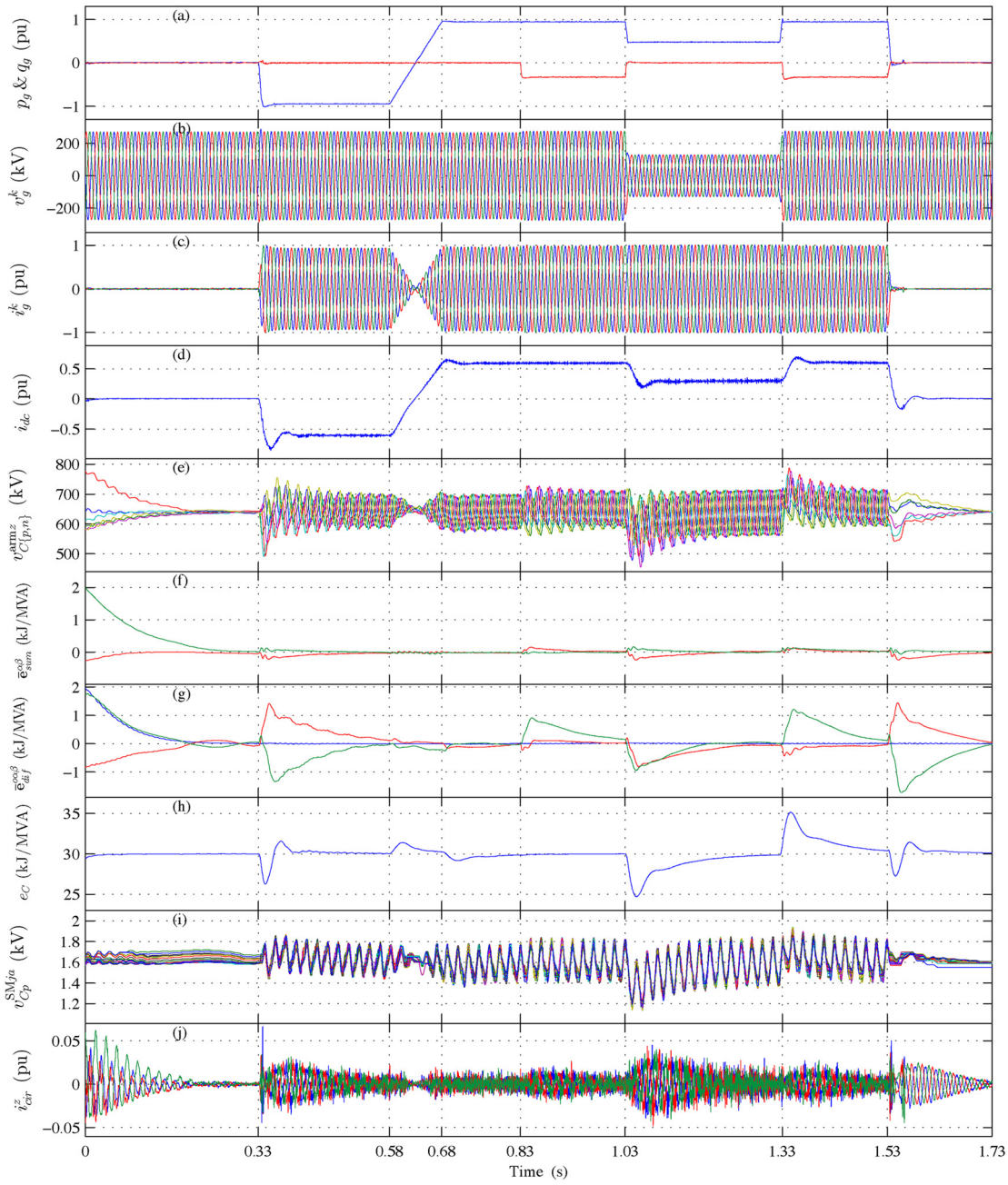

Fig. 5. (a) Active and reactive powers (blue and red lines, respectively). (b) Phase-to-ground ac voltage. (c) AC current. (d) DC current. (e) Sum of all capacitor voltages in each arm. (f) Components of the sum energy vector (horizontal balancing) $\bar{\mathbf{e}}_{\text{sum}}^{\alpha\beta}$. (g) Components of the difference energy vector (vertical balancing) $\bar{\mathbf{e}}_{\text{dif}}^{\alpha\beta}$. (h) Total converter energy. (i) Submodule capacitor voltages of the phase-*a* positive arm. (j) Circulating current.

control and the voltage balancing control under different operating conditions. In this test, the model from Sections 2 and 3 and the control system from Sections 4 and 5 are used.

The active power reference is initially set to zero; at 0.33 s, an active power step of 1000 MW is applied; then, at 0.58 s, the power flow is reversed with a 100-ms ramp from inverter to rectifier operation. The reactive power reference is set to zero and changes to 350 MVAr at 0.83 s [see active and reactive powers in Fig. 5(a)]. Two disturbances are also considered: the first one is a 300-ms voltage sag to 50% applied at 1.03 s [see Fig. 5(b)], and the second one is a shutdown of the converter performed at 1.53 s by setting the current references to zero ($\mathbf{i}_g^\star = 0$) [see Fig. 5(c)]. From the above figures, it can be seen that an accurate current control is achieved. In the control scheme, an active power priority is implemented when the current reaches its maximum value [see Fig. 5(a) during the voltage sag].

The total arm voltages are initialized to different values [see Fig. 5(e)] to show the horizontal and vertical balancing illustrated by the sum and difference energies in Fig. 5(f) and (g), respectively, whereas the total energy control is shown in Fig. 5(h). In Fig. 5(e)–(i), it is seen that all capacitor voltages and arm energies are properly controlled and balanced under the different operating conditions. Finally, Fig. 5(j) shows how the fundamental-frequency and dc components of

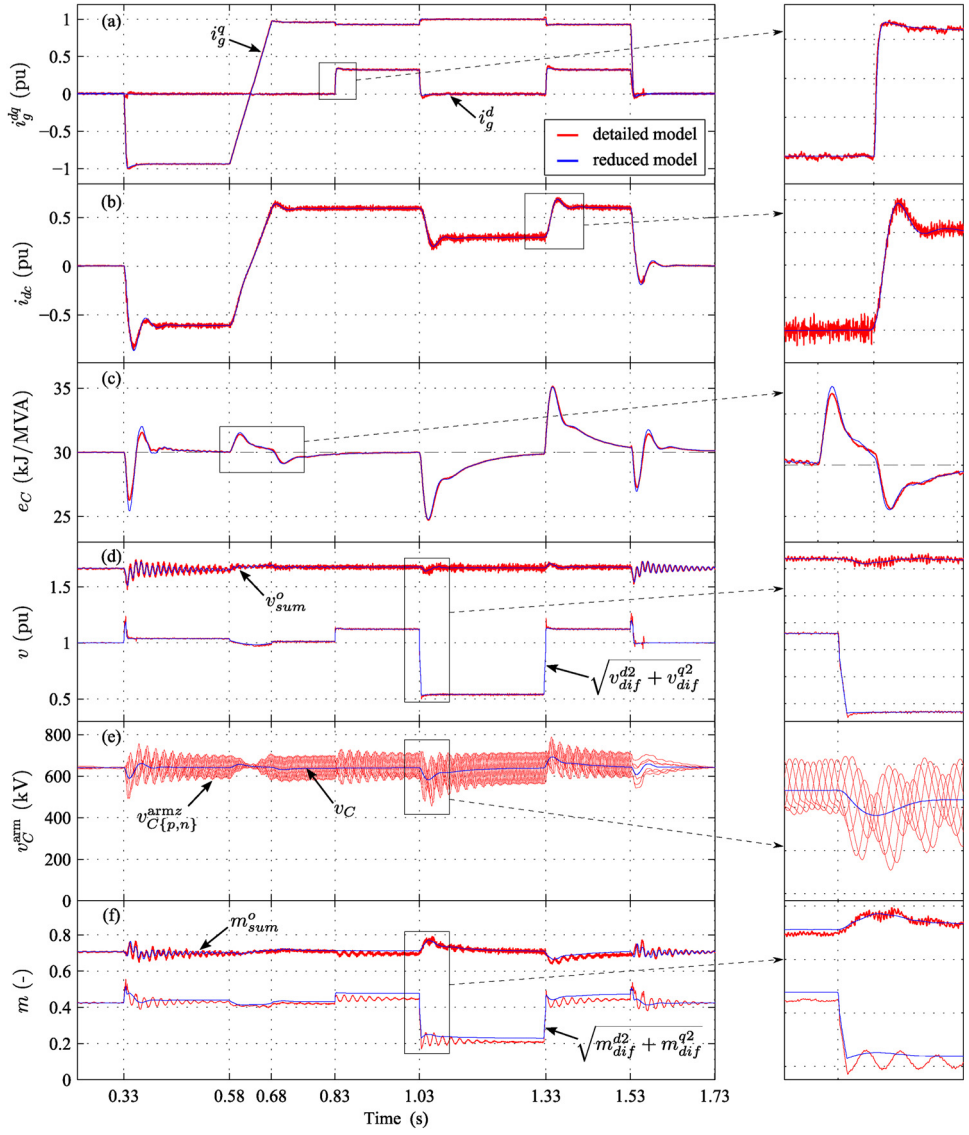

Fig. 6. Response comparison between the detailed and the reduced models under different operating conditions. (a) *D*-axis and *q*-axis currents. (b) DC current. (c) Total converter energy. (d) Components of the synthesized arm voltages. (e) Capacitor voltages. (f) Modulation indices.

the circulating current are transiently used to achieve the voltage balancing tasks, and then they are nullified in steady state.

8.2. Comparison of the detailed and reduced models

In this section, the previous test is repeated using both the detailed and the reduced models to compare their steady-state and transient responses. The trajectories of the currents and the total converter energy of both systems are almost the same [see Fig. 6(a)–(c)], which is expected because they are regulated to track the same reference signals. The sum and difference components of the arm voltages obtained from the controllers are also quite similar [see Fig. 6(d)], which reflects an appropriate representation of the MMC dynamics by the reduced model. Fig. 6(e) shows the sum of all submodule capacitor voltages in each arm $v_{C\{p,n\}}^{\mathrm{armz}}$ (detailed model) and the equivalent capacitor voltage v_C (reduced model). In the control law, the modulation indices compensate the capacitor voltage variations. Therefore, since the capacitor voltage ripples are neglected in the reduced model, its modulation indices differ from the ones obtained in the detailed model. In the modulation index m_{dif}^{z}, this difference has mostly a fundamental frequency component, which is seen as a dc offset in the magnitude $|\mathbf{m}_{\mathrm{dif}}^{\mathrm{dq}}| = \sqrt{m_{\mathrm{dif}}^{d2} + m_{\mathrm{dif}}^{q2}}$ [see Fig. 6(f)]. Other differences observed in the zoom windows on the right side of Fig. 6 are mainly due to the transient use of the circulating current by the balancing control, which is neglected in the reduced model.

A test with a three-phase fault is also presented to show the behavior of the models under a more severe disturbance. The fault is applied on the high-voltage side of the transformer, and it lasts 250 ms [see the resulting ac-side voltage in Fig. 7(a)]. During the fault, it can be observed that the capacitor voltages are properly controlled, and the ac current is limited to its maximum value (more serious faults will require the shutdown of the converter). Despite the simplifications performed in the reduced model, Fig. 7(b)–(d) show a good agreement between the transient responses of both models. To study the converter start-up and

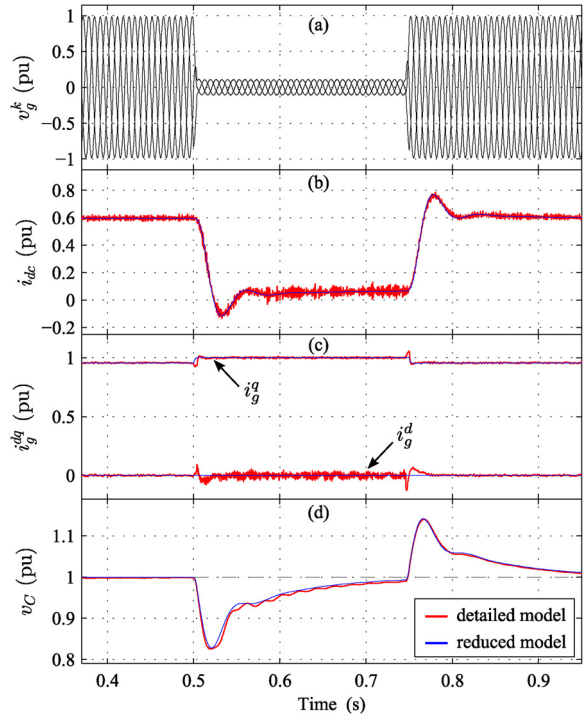

Fig. 7. Response comparison between the detailed and the reduced models under a three-phase fault. (a) AC voltage. (b) DC current. (c) *D*-axis and *q*-axis currents. (d) Equivalent capacitor voltage.

dc-side faults, it is necessary to add a blocking module to model the blocked state of the MMC (see [13,30] for a detailed description of this issue).

9. Conclusion

In this work, the modeling and control of the MMC were described in detail. Dynamic equations were obtained directly from the electrical circuit of the MMC, allowing a better understanding and representation of the converter behavior. Both a model with information on the submodule level and a reduced model for electromechanical transient simulations and small-signal analysis were developed. They were compared to evaluate and quantify the impact of the considered simplifications. The results showed that the reduced model closely matched the transient response of the more detailed version, making the reduced model suitable for large-scale power system studies where the computational cost is a challenge. The models were tested under different set-point changes and disturbances using the ac/dc converter station of the INELFE project. Differences between the traditional VSC and the MMC were also discussed to show their distinctive dc-side operating characteristics.

Acknowledgements

This work was supported in part by the Consejo Nacional de Investigaciones Científicas y Técnicas (CONICET) and in part by the Universidad Nacional del Sur (UNS).

Appendix A

The design of the ac current control is developed in this appendix. The ac current $\mathbf{i}_g$ is controlled via the difference voltage $\mathbf{v}_{dif}$, and the controller is implemented in a rotating reference frame as described in the following steps.

A.1 Discrete state-space representation of the AC current dynamics

As explained in Section 2.3, the zero-sequence component of the ac current is null; therefore, the ac current dynamics (40) is simplified to

$$\frac{1}{\Omega_B} L_t \dot{\mathbf{i}}_g^{\alpha\beta} = -R_t \mathbf{i}_g^{\alpha\beta} + \mathbf{v}_g^{\alpha\beta} - \mathbf{v}_{\text{dif}}^{\alpha\beta} \tag{124}$$

where $\mathbf{i}_g^{\alpha\beta} = [i_g^\alpha \; i_g^\beta]^T$, $\mathbf{v}_g^{\alpha\beta} = [v_g^\alpha \; v_g^\beta]^T$, and $\mathbf{v}_{\text{dif}}^{\alpha\beta} = [v_{\text{dif}}^\alpha \; v_{\text{dif}}^\beta]^T$, and the model (124) is written in per-unit values on the converter base. A state-space representation of (124) is given by

$$\dot{\mathbf{i}}_g^{\alpha\beta} = \mathbf{A}_t \mathbf{i}_g^{\alpha\beta} + \mathbf{B}_t \mathbf{v}_g^{\alpha\beta} - \mathbf{B}_t \mathbf{v}_{\text{dif}}^{\alpha\beta} \tag{125}$$

where $\mathbf{A}_t = -\frac{R_t \Omega_B}{L_t}\mathbf{I}$ and $\mathbf{B}_t = \frac{\Omega_B}{L_t}\mathbf{I}$. Then, (125) is discretized using the ZOH method obtaining

$$\mathbf{i}_{g(k+1)}^{\alpha\beta} = \mathbf{G}_t \mathbf{i}_{\text{gk}}^{\alpha\beta} + \mathbf{H}_t \mathbf{v}_{\text{gk}}^{\alpha\beta} - \mathbf{H}_t \mathbf{v}_{\text{difk}}^{\alpha\beta} \tag{126}$$

where the matrices of the discrete system are calculated as $\mathbf{G}_t = e^{\mathbf{A}_t T_s}$ and $\mathbf{H}_t = \int_0^{T_s} e^{\mathbf{A}_t \tau} d\tau \mathbf{B}_t$ [39].

A.2 Transformation to a rotating reference frame

To simplify the control design, the ac current dynamics (126) is transformed to the *dq* synchronous reference frame. First, the discrete Park transformation at the sample times k and $k+1$ is introduced

$$\mathbf{P}_k = \begin{bmatrix} \cos\theta_k & -\sin\theta_k \\ \sin\theta_k & \cos\theta_k \end{bmatrix} \tag{127}$$

$$\mathbf{P}_{k+1} = \begin{bmatrix} \cos\theta_{k+1} & -\sin\theta_{k+1} \\ \sin\theta_{k+1} & \cos\theta_{k+1} \end{bmatrix}. \tag{128}$$

The transformation $\mathbf{P}$ rotates at the system angular frequency Ω_B; then, $\theta_k = \Omega_B t_k$ and $\theta_{k+1} = \Omega_B t_{k+1} = \Omega_B (t_k + T_s)$. Therefore, the following matrix can be defined using (127) and (128)

$$\boldsymbol{\Omega} = \mathbf{P}_{k+1}\mathbf{P}_k^{-1} = \begin{bmatrix} \cos(\Omega_B T_s) & -\sin(\Omega_B T_s) \\ \sin(\Omega_B T_s) & \cos(\Omega_B T_s) \end{bmatrix}. \tag{129}$$

For a generic vector $\mathbf{f}^{\alpha\beta}$, it is verified $\mathbf{f}_k^{\mathrm{dq}} = \mathbf{P}_k \mathbf{f}_k^{\alpha\beta}$ and $\mathbf{f}_{k+1}^{\mathrm{dq}} = \mathbf{P}_{k+1}\mathbf{f}_{k+1}^{\alpha\beta}$; consequently, applying the Park transformations (127) and (128) to the system (126) results in

$$\mathbf{P}_{k+1}^{-1}\mathbf{i}_{g(k+1)}^{\mathrm{dq}} = \mathbf{G}_t\mathbf{P}_k^{-1}\mathbf{i}_{\mathrm{gk}}^{\mathrm{dq}} + \mathbf{H}_t\mathbf{P}_k^{-1}\mathbf{v}_{\mathrm{gk}}^{\mathrm{dq}} - \mathbf{H}_t\mathbf{P}_k^{-1}\mathbf{v}_{\mathrm{difk}}^{\mathrm{dq}}. \tag{130}$$

Finally, premultiplying (130) by $\mathbf{P}_{k+1}$ yields

$$\mathbf{i}_{g(k+1)}^{\mathrm{dq}} = \overline{\mathbf{G}}_t\mathbf{i}_{\mathrm{gk}}^{\mathrm{dq}} + \overline{\mathbf{H}}_t\mathbf{v}_{\mathrm{gk}}^{\mathrm{dq}} - \overline{\mathbf{H}}_t\mathbf{v}_{\mathrm{difk}}^{\mathrm{dq}} \tag{131}$$

where $\overline{\mathbf{G}}_t = \mathbf{P}_{k+1}\mathbf{G}_t\mathbf{P}_k^{-1}$ and $\overline{\mathbf{H}}_t = \mathbf{P}_{k+1}\mathbf{H}_t\mathbf{P}_k^{-1}$.

A.3 Computational delay compensation

Similar to what is described in Section 4.2.2, the computational delay can be considered in the control design by defining an auxiliary control input as follows

$$\mathbf{v}_{\mathrm{dif}(k+1)}^{\alpha\beta} = \mathbf{n}_{\mathrm{difk}}^{\alpha\beta}. \tag{132}$$

Eq. (132) is transformed to the *dq* reference frame proceeding as in (130), obtaining

$$\mathbf{v}_{\mathrm{dif}(k+1)}^{\mathrm{dq}} = \Omega\mathbf{n}_{\mathrm{difk}}^{\mathrm{dq}}. \tag{133}$$

A.4 Extended model for the control design

In the *dq* synchronous reference frame, the fundamental frequency components of the ac current references are transformed to constant (or dc) signals, which can be easily tracked using a PI controller. The integrators of two PI controllers, one for the *d*-axis and another one for the *q*-axis, are discretized and written in vector form as follows

$$\mathbf{q}_{g(k+1)} = \mathbf{q}_{\mathrm{gk}} + T_s\mathbf{e}_{\mathrm{gk}}^{\mathrm{dq}} \tag{134}$$

where $\mathbf{e}_{\mathrm{gk}}^{\mathrm{dq}} = \mathbf{i}_{\mathrm{gk}}^{\mathrm{dq}} - \mathbf{i}_{\mathrm{gk}}^{\star\mathrm{dq}}$ is the tracking error. Then, an extended model is obtained by combining the ac current model (131), the computational delay model (133), and the PI control integrators (134)

$$\mathbf{w}_{g(k+1)} = \mathbf{A}_{\mathrm{ge}}\mathbf{w}_{\mathrm{gk}} + \mathbf{B}_{\mathrm{ge}}\mathbf{n}_{\mathrm{difk}}^{\mathrm{dq}} + \mathbf{B}_{\mathrm{ge}}^{v}\mathbf{v}_{\mathrm{gk}}^{\mathrm{dq}} - \mathbf{B}_{\mathrm{ge}}^{r}\mathbf{i}_{\mathrm{gk}}^{\star\mathrm{dq}} \tag{135}$$

with state vector

$$\mathbf{w}_{\mathrm{gk}} = \begin{bmatrix} \mathbf{i}_{\mathrm{gk}}^{\mathrm{dq}} & \mathbf{v}_{\mathrm{difk}}^{\mathrm{dq}} & \mathbf{q}_{\mathrm{gk}} \end{bmatrix}^T \tag{136}$$

and matrices

$$\mathbf{A}_{\mathrm{ge}} = \begin{bmatrix} \overline{\mathbf{G}}_t & -\overline{\mathbf{H}}_t & \mathbf{0} \\ \mathbf{0} & \mathbf{0} & \mathbf{0} \\ T_s\mathbf{I} & \mathbf{0} & \mathbf{I} \end{bmatrix} \tag{137}$$

$$\mathbf{B}_{\mathrm{ge}} = [\mathbf{0} \quad \boldsymbol{\Omega} \quad \mathbf{0}]^T \tag{138}$$

$$\mathbf{B}_{\mathrm{ge}}^{v} = [\overline{\mathbf{H}}_t \quad \mathbf{0} \quad \mathbf{0}]^T \tag{139}$$

$$\mathbf{B}_{\mathrm{ge}}^{r} = [\mathbf{0} \quad \mathbf{0} \quad T_s\mathbf{I}]^T. \tag{140}$$

A.5 Control law

The control law consists of feedback and feedforward terms, and it is designed using a state-space approach. In a PI controller, the integral action modifies the integrator value to achieve a zero steady-state tracking error when disturbances such as changes in either the current reference or the ac grid voltage occur. Because these disturbances are measured, the steady-state integrator value can be calculated beforehand as a function of the current reference $\mathbf{i}_g^{\star\mathrm{dq}}$ and the ac voltage $\mathbf{v}_g^{\mathrm{dq}}$ (i.e., in a feedforward manner), consequently improving the control performance and avoiding high gains in the PI controller to compensate these disturbances. Firstly, the following feedback control law is considered by measuring the states (136) – the feedforward term will be calculated afterwards–

$$\mathbf{n}_{\mathrm{difk}}^{\mathrm{dq}} = -\mathbf{K}_t\mathbf{w}_{\mathrm{gk}}. \tag{141}$$

The closed-loop system is obtained substituting (141) into (135) yielding

$$\mathbf{w}_{g(k+1)} = (\mathbf{A}_{\mathrm{ge}} - \mathbf{B}_{\mathrm{ge}}\mathbf{K}_t)\mathbf{w}_{\mathrm{gk}} + \mathbf{B}_{\mathrm{ge}}^{v}\mathbf{v}_{\mathrm{gk}}^{\mathrm{dq}} - \mathbf{B}_{\mathrm{ge}}^{r}\mathbf{i}_{\mathrm{gk}}^{\star\mathrm{dq}}. \tag{142}$$

As in Section 4.2.5, the feedback gain matrix $\mathbf{K}_t$ is designed to obtain a desired closed-loop matrix $(\mathbf{A}_{\mathrm{ge}} - \mathbf{B}_{\mathrm{ge}}\mathbf{K}_t)$ using the LQR method.

In steady-state, the values of the state variables $\mathbf{w}_g$ are constant and satisfy

$$\mathbf{w}_{gss} = \mathbf{w}_{g(k+1)} = \mathbf{w}_{gk}. \tag{143}$$

Therefore, from (142) and considering (143), the steady-state value $\mathbf{w}_{gss}$ is obtained as follows

$$\mathbf{w}_{gss} = \mathbf{J}(\mathbf{B}_{ge}^{v}\mathbf{v}_{gk}^{dq} - \mathbf{B}_{ge}^{r}\mathbf{i}_{gk}^{\star dq}) \tag{144}$$

where $\mathbf{J} = (\mathbf{I} - \mathbf{A}_{ge} + \mathbf{B}_{ge}\mathbf{K}_t)^{-1}$. Expanding (144), the following sub-matrices $\mathbf{J}_{ij}$ can be defined

$$\begin{bmatrix} \mathbf{i}_{gss}^{dq} \\ \mathbf{v}_{difss}^{dq} \\ \mathbf{q}_{gss} \end{bmatrix} = \begin{bmatrix} \mathbf{J}_{11} & \mathbf{J}_{12} & \mathbf{J}_{13} \\ \mathbf{J}_{21} & \mathbf{J}_{22} & \mathbf{J}_{23} \\ \mathbf{J}_{31} & \mathbf{J}_{32} & \mathbf{J}_{33} \end{bmatrix} \begin{bmatrix} \overline{\mathbf{H}}_t\mathbf{v}_{gk}^{dq} \\ \mathbf{0} \\ -T_s\mathbf{i}_{gk}^{\star dq} \end{bmatrix}. \tag{145}$$

Then, from the third row of (145), the steady-state integrator value is calculated as

$$\mathbf{q}_{gss} = \mathbf{J}_{31}\overline{\mathbf{H}}_t\mathbf{v}_{gk}^{dq} - T_s\mathbf{J}_{33}\mathbf{i}_{gk}^{\star dq}. \tag{146}$$

The value $\mathbf{q}_{gss}$ is added, in a feedforward manner, to the integrator output (i.e., to the state variable $\mathbf{q}_{gk}$) in the control law (141) as follows

$$\mathbf{n}_{difk}^{dq} = -[\mathbf{K}_{ti} \quad \mathbf{K}_{tv} \quad \mathbf{K}_{tm}] \begin{bmatrix} \mathbf{i}_{gk}^{dq} \\ \mathbf{v}_{difk}^{dq} \\ \mathbf{q}_{gk} + \mathbf{q}_{gss} \end{bmatrix} \tag{147}$$

where the feedback gain matrix has been divided into the following sub-matrices $\mathbf{K}_t = [\mathbf{K}_{ti}\,\mathbf{K}_{tv}\,\mathbf{K}_{tm}]$. Finally, rearranging (147), the complete control law is given as

$$\mathbf{n}_{difk}^{dq} = -\mathbf{K}_t\mathbf{w}_{gk} - \mathbf{K}_s\mathbf{v}_{gk}^{dq} - \mathbf{K}_r\mathbf{i}_{gk}^{\star dq} \tag{148}$$

where $\mathbf{K}_s = \mathbf{K}_{tm}\mathbf{J}_{31}\overline{\mathbf{H}}_t$ and $\mathbf{K}_r = -T_s\mathbf{K}_{tm}\mathbf{J}_{33}$. In (148), the first term is the feedback part, and the last two terms are the feedforward compensation.

References

[1] C. Gavriluta, I. Candela, C. Citro, A. Luna, P. Rodriguez, Design considerations for primary control in multi-terminal VSC–HVDC grids, Electr. Power Syst. Res. 122 (2015) 33–41.

[2] M. Perez, S. Bernet, J. Rodriguez, S. Kouro, R. Lizana, Circuit topologies, modeling, control schemes, and applications of modular multilevel converters, IEEE Trans. Power Electron. 30 (1) (2015) 4–17.

[3] E. Prieto-Araujo, A. Junyent-Ferre, C. Collados-Rodriguez, G. Clariana-Colet, O. Gomis-Bellmunt, Control design of modular multilevel converters in normal and AC fault conditions for HVDC grids, Electr. Power Syst. Res. 152 (2017) 424–437.

[4] A. Antonio-Ferreira, C. Collados-Rodriguez, O. Gomis-Bellmunt, Modulation techniques applied to medium voltage modular multilevel converters for renewable energy integration: a review, Electr. Power Syst. Res. 155 (2018) 21–39.

[5] I.M. Sanz, B. Chaudhuri, G. Strbac, Inertial response from offshore wind farms connected through DC grids, IEEE Trans. Power Syst. 30 (3) (2015) 1518–1527.

[6] G. Stamatiou, M. Bongiorno, Power-dependent droop-based control strategy for multi-terminal HVDC transmission grids, IET Gener. Transm. Distrib. 11 (2) (2017) 383–391.

[7] K. Rouzbehi, W. Zhang, J.I. Candela, A. Luna, P. Rodriguez, Unified reference controller for flexible primary control and inertia sharing in multi-terminal voltage source converter-HVDC grids, IET Gener. Transm. Distrib. 11 (3) (2017) 750–758.

[8] S. Akkari, J. Dai, M. Petit, X. Guillaud, Interaction between the voltage-droop and the frequency-droop control for MT–HVDC systems, IET Gener. Transm. Distrib. 10 (6) (2016) 1345–1352.

[9] D. Soto-Sanchez, T. Green, Control of a modular multilevel converter-based HVDC transmission system, European Conf. on Power Electronics and Applications (2011) 1–10.

[10] H. Yang, Y. Dong, W. Li, X. He, Average-value model of modular multilevel converters considering capacitor voltage ripple, IEEE Trans. Power Deliv. 32 (2) (2017) 723–732.

[11] G. Bergna Diaz, J.A. Suul, S. D'Arco, Small-signal state-space modeling of modular multilevel converters for system stability analysis, IEEE Energy Conversion Congress and Exposition (2015) 5822–5829.

[12] S. Rohner, J. Weber, S. Bernet, Continuous model of modular multilevel converter with experimental verification, IEEE Energy Conversion Congress and Exposition (2011) 4021–4028.

[13] N. Ahmed, L. Angquist, S. Norrga, A. Antonopoulos, L. Harnefors, H.P. Nee, A computationally efficient continuous model for the modular multilevel converter, IEEE J. Emerg. Sel. Top. Power Electron. 2 (4) (2014) 1139–1148.

[14] S. Wenig, F. Rojas, K. Schonleber, M. Suriyah, T. Leibfried, Simulation framework for DC grid control and ACDC interaction studies based on modular multilevel converters, IEEE Trans. Power Deliv. 31 (2) (2016) 780–788.

[15] S. Samimi, F. Gruson, P. Delarue, F. Colas, M.M. Belhaouane, X. Guillaud, MMC stored energy participation to the DC bus voltage control in an HVDC link, IEEE Trans. Power Deliv. 31 (4) (2016) 1710–1718.

[16] G. Bergna-Diaz, J. Freytes, X. Guillaud, S. D'Arco, J.A. Suul, Generalized voltage-based state-space modeling of modular multilevel converters with constant equilibrium in steady state, IEEE J. Emerg. Sel. Top. Power Electron. 6 (June (2)) (2018) 707–725.

[17] G. Bergna-Diaz, J.A. Suul, S. D'Arco, Energy-based state-space representation of modular multilevel converters with a constant equilibrium point in steady-state operation, IEEE Trans. Power Electron. 33 (June (6)) (2018) 4832–4851.

[18] A. Jamshidifar, D. Jovcic, Small-signal dynamic dq model of modular multilevel converter for system studies, IEEE Trans. Power Deliv. 31 (1) (2016) 191–199.

[19] G. Bergna, J.A. Suul, S. D'Arco, State-space modelling of modular multilevel converters for constant variables in steady-state, IEEE Workshop Control and Modeling for Power Electr. (2016) 1–9.

[20] J. Freytes, L. Papangelis, H. Saad, P. Rault, T.V. Cutsem, X. Guillaud, On the modeling of MMC for use in large scale dynamic simulations, Power Systems Comput. Conference (2016) 1–7.

[21] J. Peralta, H. Saad, S. Dennetiere, J. Mahseredjian, S. Nguefeu, Detailed and averaged models for a 401-level MMC–HVDC system, IEEE Trans. Power Deliv. 27 (3) (2012) 1501–1508.

[22] H. Saad, J. Peralta, S. Dennetiere, J. Mahseredjian, J. Jatskevich, J. Martinez, A. Davoudi, M. Saeedifard, V. Sood, X. Wang, J. Cano, A. Mehrizi-Sani, Dynamic averaged and simplified models for MMC-based HVDC transmission systems, IEEE Trans. Power Deliv. 28 (3) (2013) 1723–1730.

[23] S. Liu, Z. Xu, W. Hua, G. Tang, Y. Xue, Electromechanical transient modeling of modular multilevel converter based multi-terminal HVDC systems, IEEE Trans. Power Syst. 29 (1) (2014) 72–83.

[24] N.T. Trinh, M. Zeller, K. Wuerflinger, I. Erlich, Generic model of MMC–VSC–HVDC for interaction study with AC power system, IEEE Trans. Power Syst. 31 (1) (2016) 27–34.

[25] R. Irnawan, F.F. da Silva, C.L. Bak, T.C. Bregnhøj, Evaluation of half-bridge modular multilevel converter model for VSC–HVDC transient stability studies, IET Inter. Conf. on AC and DC Power Transmission (2017) 1–6.

[26] K. Longze, Z. Lin, L. Fangyuan, Electromechanical modelling of modular multilevel converter based HVDC system and its application, IEEE Conf. on Energy Internet and Energy System Integration (2017) 1–6.

[27] H. Saad, S. Dennetiere, J. Mahseredjian, P. Delarue, X. Guillaud, J. Peralta, S. Nguefeu, Modular multilevel converter models for electromagnetic transients, IEEE Trans. Power Deliv. 29 (3) (2014) 1481–1489.

[28] H. Saad, J. Mahseredjian, S. Dennetiere, S. Nguefeu, Interactions studies of HVDC–MMC link embedded in an AC grid, Electr. Power Syst. Res. 138 (2016) 202–209.

[29] W. Wang, M. Barnes, O. Marjanovic, O. Cwikowski, Impact of DC breaker systems on multiterminal VSC–HVDC stability, IEEE Trans. Power Deliv. 31 (2) (2016) 769–779.

[30] A. Beddard, C.E. Sheridan, M. Barnes, T.C. Green, Improved accuracy average value models of modular multilevel converters, IEEE Trans. Power Deliv. 31 (5) (2016) 2260–2269.

[31] Y. Li, G. Tang, J. Ge, Z. He, H. Pang, J. Yang, Y. Wu, Modeling and damping control of modular multilevel converter based DC grid, IEEE Trans. Power Syst. 33 (1) (2018) 723–735.

[32] D. Ludois, G. Venkataramanan, Simplified terminal behavioral model for a modular multilevel converter, IEEE Trans. Power Electron. 29 (4) (2014) 1622–1631.

[33] S. Dennetiere, H. Saad, B. Clerc, J. Mahseredjian, Setup and performances of the real-time simulation platform connected to the INELFE control system, Electr. Power Syst. Res. 138 (2016) 180–187.

[34] J. Wang, R. Burgos, D. Boroyevich, Switching-cycle state-space modeling and

control of the modular multilevel converter, IEEE J. Emerg. Sel. Top. Power Electron. 2 (4) (2014) 1159–1170.
[35] Y. Wan, S. Liu, J. Jiang, Generalised analytical methods and current-energy control design for modular multilevel cascade converter, IET Power Electron. 6 (3) (2013) 495–504.
[36] S. Cui, S. Kim, J.-J. Jung, S.-K. Sul, A comprehensive cell capacitor energy control strategy of a modular multilevel converter (MMC) without a stiff DC bus voltage source, IEEE Applied Power Electronics Conference and Exposition (2014) 602–609.
[37] J. Li, G. Konstantinou, H.R. Wickramasinghe, J. Pou, X. Wu, X. Jin, Investigation of MMC–HVDC operating region by circulating current control under grid imbalances, Electr. Power Syst. Res. 152 (2017) 211–222.
[38] A.E. Leon, S.J. Amodeo, Energy balancing improvement of modular multilevel converters under unbalanced grid conditions, IEEE Trans. Power Electron. 32 (8) (2017) 6628–6637.
[39] K. Ogata, Discrete-Time Control Systems, 2nd ed., Prentice-Hall, Englewood Cliffs, NJ, USA, 1995.
[40] P. Rodriguez, A. Luna, R. Muñoz-Aguilar, I. Etxeberria-Otadui, R. Teodorescu, F. Blaabjerg, A stationary reference frame grid synchronization system for three-phase grid-connected power converters under adverse grid conditions, IEEE Trans. Power Electron. 27 (1) (2012) 99–112.
[41] A.E. Leon, J.A. Solsona, Performance improvement of full-converter wind turbines under distorted conditions, IEEE Trans. Sustain. Energy 4 (3) (2013) 652–660.
[42] F.L. Lewis, D.L. Vrabie, V.L. Syrmos, Optimal Control, 3rd ed., John Wiley & Sons, Hoboken, NJ, USA, 2012.
[43] T.K. Vrana, J. Beerten, R. Belmans, O.B. Fosso, A classification of DC node voltage control methods for HVDC grids, Electr. Power Syst. Res. 103 (2013) 137–144.
[44] M. Saeedifard, R. Iravani, Dynamic performance of a modular multilevel back-to-back HVDC system, IEEE Trans. Power Deliv. 25 (4) (2010) 2903–2912.
[45] V. Blasco, V. Kaura, A new mathematical model and control of a three-phase AC–DC voltage source converter, IEEE Trans. Power Electron. 12 (1) (1997) 116–123.